Fall 2013

Synthesis and device applications of graphitic nanomaterials

Ahmad Umair
University of Iowa

Recommended Citation

Umair, Ahmad. "Synthesis and device applications of graphitic nanomaterials." PhD (Doctor of Philosophy) thesis, University of Iowa, 2013.
https://doi.org/10.17077/etd.jvi9gm3t

SYNTHESIS AND DEVICE APPLICATIONS OF GRAPHITIC NANOMATERIALS

by

Ahmad Umair

A thesis submitted in partial fulfillment
of the requirements for the Doctor of
Philosophy degree in Electrical and Computer Engineering
in the Graduate College of
The University of Iowa

December 2013

Thesis Supervisor: Adjunct Assistant Professor Hassan Raza

Graduate College
The University of Iowa
Iowa City, Iowa

CERTIFICATE OF APPROVAL

_____

PH.D. THESIS

_____

This is to certify that the Ph.D. thesis of

Ahmad Umair

has been approved by the Examining Committee
for the thesis requirement for the Doctor of Philosophy
degree in Electrical and Computer Engineering at the December 2013
graduation.

Thesis Committee: _____
                   Hassan Raza, Thesis Supervisor

                   _____
                   David R. Andersen

                   _____
                   Thomas F. Boggess

                   _____
                   John P. Prineas

                   _____
                   Markus Wohlgenannt

To my loving family.

ACKNOWLEDGMENTS

ABSTRACT

This thesis is focused on two topics: (i) synthesis and characterization of bilayer graphene and pyrolytic carbon by atmospheric pressure chemical vapor deposition, and (ii) application of graphene in the fabrication of a buckyball memory device.

Monolayer and bilayer graphene are semi-metal with zero bandgap. One can induce a bandgap in bilayer graphene by applying a gate voltage in the stacking direction. Thus, bandgap and Fermi level in bilayer graphene can be controlled simultaneously with a double-gate device, making it a useful material for future semiconducting applications. Controlled synthesis of bilayer graphene would be the first step to fabricate bilayer graphene based devices. In this context, we report a uniform and low-defect synthesis of bilayer graphene on evaporated nickel films. Ultra-fast cooling is employed to control the number of layers and sample uniformity. The process is self-limiting, which leads to bilayer graphene synthesis over a wide range of growth-time and precursor flow-rate.

Pryolytic carbon is another important carbon nanomaterial, due to its diverse applications in electronic and biomedical engineering. We employ chemical vapor deposition with ultra-fast cooling technique to synthesize pyrolytic carbon. Furthermore, we elucidate a method to calculate the in-plane crystal size by using Raman spectroscopy.

Finally, the use of bilayer graphene in a write-once read-many memory device has been demonstrated. The device showed irreversible switching from low-resistance to high-resistance state, with hysteresis in the transport characteristics. The control sample showed random switching and hysteresis due to electromigration of metal atoms into the active material of the device. We attribute the reliability and performance of the reported device to the ultra-smooth graphene contacts, which additionally inhibits electromigration from the underlying metallic film. Moreover, the memory device showed excellent endurance and retention characteristics.

TABLE OF CONTENTS

LIST OF TABLES

Table

LIST OF FIGURES

CHAPTER 1

INTRODUCTION

Novel materials to replace silicon for future nanoelectronics have been studied extensively as the current CMOS technology is reaching its scaling limits [1]. Nanomaterials based on sp^2 hybridized carbon atoms are at the forefront in this concern. Graphene can be considered as the basis to understand the properties of other carbon nanomaterials, by applying proper boundary conditions, despite the fact it was discovered most recent amongst them. It can be imagined to wrap in 0-D, roll in 1-D and stack in 2-D to form fullerene molecules, carbon nanotubes and graphite, respectively, as shown in Figure 1-1. If graphene layers are stacked in the stacking direction, with the lack of a particular stacking sequence and small in-plane crystal size, the 3-D form is called pyrolytic carbon. All of these materials have unique electrical, mechanical, optical and magnetic properties, which make them important for future nanotechnology applications.
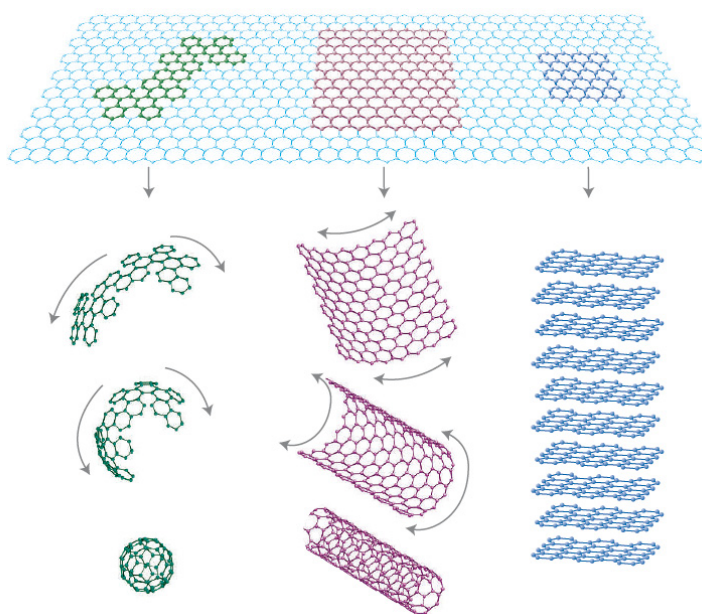
Figure 1-1   Various allotropic forms of sp^2 carbon [2].

Graphene was discovered in 2004 by mechanical exfoliation of graphite (also known as scotch tape method) [3]. Earlier, it was predicted that thermal fluctuations would cause lattice dislocations in a 2-D material and destabilize the structure [2]. After its discovery, it has been studied extensively and some excellent physical properties have been reported.

Graphene has high carrier mobility at room temperature. The maximum value of carrier mobility reported for suspended and unsuspended graphene are ~230,000 and ~30,000 cm^2 V^{-1} s^{-1} respectively. Whereas, maximum reported value of electron mobility in silicon is ~1,400 cm^2 V^{-1} s^{-1} [4]. Moreover, it shows ballistic conduction with mean free paths of the order of micrometers [2,4]. Graphene exhibits impressive breakdown current density of the order of 10^8 A cm^{-2}, which is approximately a thousand times greater than copper [5]. These features make graphene a perfect candidate for future electronic devices as it would provide high current density, high speed and low power consumption.

It has high optical transmittance i.e. absorbing ~3% of the visible light [6]. Thus, graphene is a perfect candidate for transparent electronics and solar cells. It has breaking strength of 40 N/m, which is almost 200 times greater than steel [7]. Moreover, the Young's modulus is ~3 GPa. These properties make it favorable for micro-electro-mechanical devices and flexible electronics. Furthermore, graphene is impermeable material to even helium atoms [8] and this feature, along with its mechanical strength, can be explored to avoid the electromigration problem by covering metallic electrodes with graphene.

Electronic properties of graphene

Monolayer graphene consists of carbon atoms arranged in a 2-D honeycomb crystal structure, as shown in Figure 1-2(a). Each carbon atom has three sp^2 hybridized and one p_z orbitals. The sp^2 hybridized orbitals of each carbon atom forms σ-bonds with

the three adjacent carbon atoms. The σ-bonds are the strongest covalent bonds and are responsible for the mechanical properties of graphene. The p_z orbital of each carbon atom forms π-bond in which electrons are delocalized, thus responsible for its electrical properties. When two or more monolayers are stacked, multilayer graphene is formed. The three most common stacking arrangements are AB (Bernal), ABC (rhombohedral) and AA (hexagonal). The most abundant configuration is Bernal stacking that can be thought of as two stacked graphene sheets with one layer rotated 60° relative to the other. Bernal-stacked bilayer graphene (BLG) is shown in Figure 1-2(b,c), with four atoms per unit cell [9].
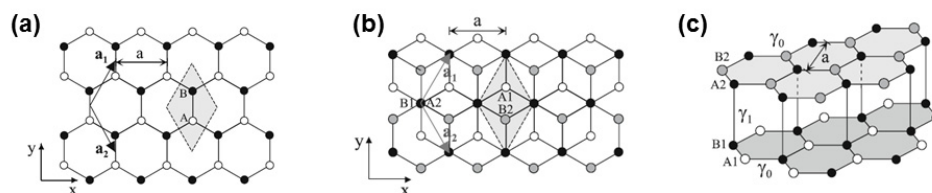
Figure 1-2   Crystal structure of monolayer and bilayer graphene. (a) Honeycomb structure of monolayer graphene. The unit cell is represented by shaded region containing two atoms A and B, (b,c) Top view and side view of crystal structure of Bernal stacked bilayer graphene, respectively. The shaded region in (b) represents unit cell with four atoms, two from each layer. Parameters γ_0 and γ_1 are nearest neighboring coupling in same and different layers, respectively [9].

The band structure of monolayer graphene obtained from tight-binding model is shown in Figure 1-3(a,b). The two energy bands i.e. conduction band (E_+) and valence band (E_-), meet at six points in the reciprocal space, thus graphene has zero bandgap. Each of these points is shared by three adjacent Brillouin zone. Therefore, each Brillouin zone fundamentally has two points labeled K_+ and K_-, also called Dirac points. The band structure of bilayer graphene is shown in Figure 1-3(c), which shows that it also has zero

bandgap. The two sub-bands in each conduction and valence bands are separated by an amount equal to the interlayer coupling parameter (γ_1). An interesting feature arises in the bandgap of bilayer graphene when two sub-lattice sites are at different energies e.g. by doping or electrostatic gating. It leads to the formation of bandgap at Dirac points, as depicted in Figure 1-3(d) [9,10]. This feature makes bilayer graphene an important material to be considered for future gate-controlled semiconducting devices. As more layers are stacked, the band structure becomes more complex with the addition of more sub-bands and finally resembles to graphite band structure for ~10-layer graphene [2,9].
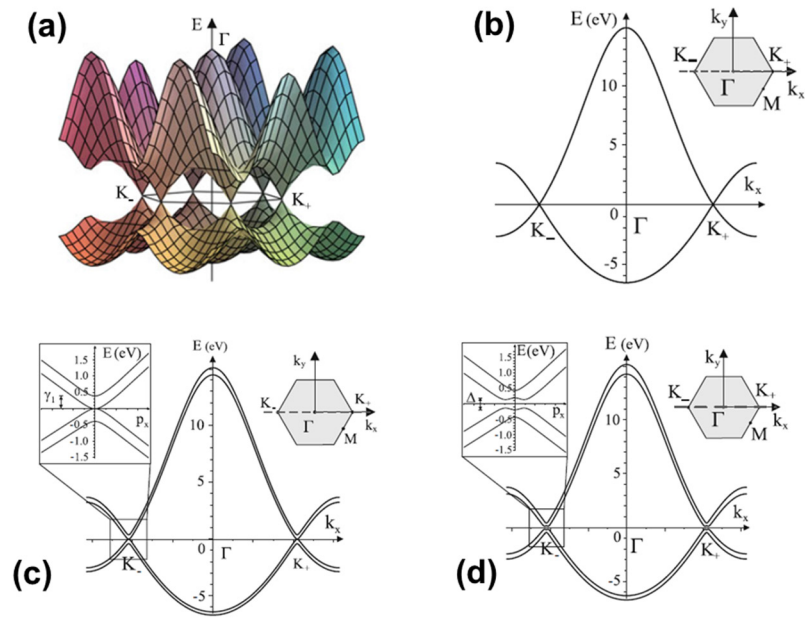
Figure 1-3   Band structure of monolayer and bilayer graphene. (a) Band structure of monolayer graphene in first Brillouin zone, obtained from tight-binding model. The conduction and valence bands touch at six corners of the Brillouin zone, (b) Cut through of the first Brillouin zone of monolayer graphene, along the k_x axis, (c) The band structure of bilayer graphene, along the k_x axis in the Brillouin zone. The inset shows the band structure in the vicinity of the Dirac points, (d) The band structure of bilayer graphene in the presence of symmetry breaking between two layers, along the k_x axis. The inset shows the band structure in the vicinity of the Dirac points [9].

The effect of gate electric field on the conduction through monolayer graphene is shown in Figure 1-4(a) [2]. The transport is ambipolar and carriers can be tuned between electrons and holes by applying positive and negative gate voltages, respectively. Ambipolar effect in a few-layer graphene at various temperatures is shown in Figure 1-4(b). The shift in the ρ-V_g peak to the right may suggest that the intrinsic carrier concentration is dominated by holes, but it is due to adsorbed water molecules on the surface of SiO_2 and graphene [3].
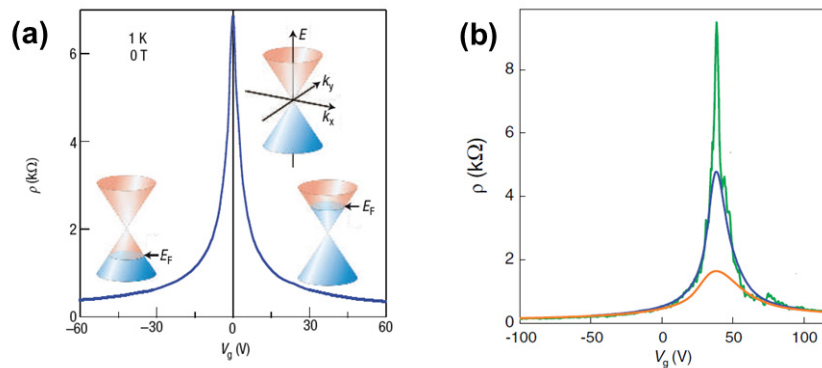
Figure 1-4   The effect of gate field on conduction through graphene. (a) Conduction through monolayer graphene under the applied gate bias. The insets show its conical low-energy spectrum E(k), indicating changes in the position of the Fermi energy E_F with changing gate voltage. The rapid decrease in resistivity on adding charge carriers indicates their high mobility, (b) Conduction through few-layer graphene under the applied gate bias at T = 5, 70 and 273 K. The temperature increases from top curve to bottom [2,3].

Graphene characterization

Various techniques have been used to characterize graphene. The most common techniques are: Raman spectroscopy, optical microscopy and electron microscopy.

Raman Spectroscopy

Raman spectroscopy is a non-destructive technique and has been widely used to characterize carbon based materials [9,11-14]. Different parameters e.g. number of layers, defect density, crystal length and stacking order can be determined from the Raman spectrum of graphene. The most prominent bands in the Raman spectrum of graphene are D, G and 2D bands. The D band is induced by defects i.e. missing atoms or impurities, and is centered ~1350 cm^{-1}. It is associated to the optical-phonons near the Dirac points. The G and 2D bands are centered at ~1580 and ~2700 cm^{-1}, respectively. The G band is the most common feature in all the graphitic materials and is originated from zone-centered in-plane optical-phonons. The 2D band (also known as G′ band), located almost double the frequency of D band, and is due to the two-phonon resonance process involving the phonons near the Dirac points.

The Raman spectra of monolayer graphene, bilayer graphene and graphite are shown in Figure 1-5. The I_D/I_G ratio can be used to determine the in-plane crystal size (L_a) by the relation $I_D/I_G = A/L_a$, where A is a constant depending on the laser excitation
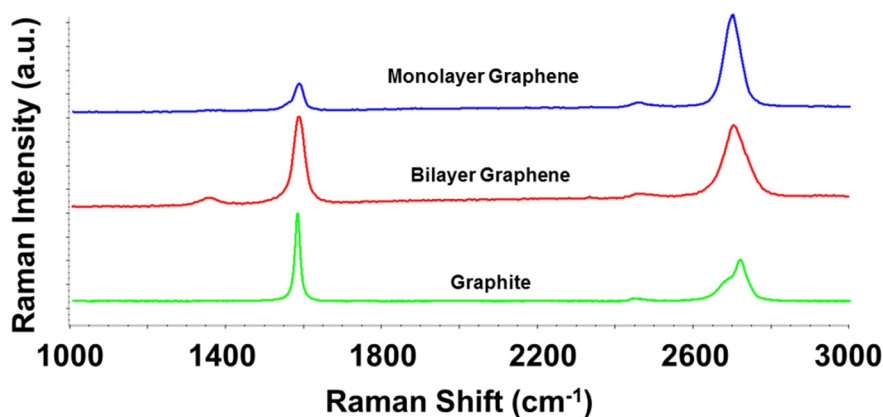
Figure 1-5   Raman spectra of graphene. The three main peaks in the spectrum are D, G and 2D, located at ~1350, 1580 and 2700 cm^{-1}, respectively. The ratio of I_{2D}/I_G peak intensities are ~1, <<1 and >>1 for bilayer graphene, monolayer graphene and graphite, respectively.

energy [9,11]. Similarly, the I_{2D}/I_G ratio can be correlated to the number of layer of graphene [9,11-13,15,16]. For monolayer graphene I_{2D}/I_G is usually a large quantity. For bilayer graphene I_{2D}/I_G is around unity and as the number of layers increases the ratio gets decreased.

Further details about Raman spectroscopy and various Raman processes in graphene related systems are discussed in Appendix A.

Optical microscopy

Graphene can be viewed on SiO_2 substrate due to optical contrast, which led to the rapid progress in this area. For the green light, having frequency in the middle of visible range and most comfortable for eyes, graphene can be visualized on ~90 and ~300 nm SiO_2 films [9]. An optical image containing monolayer, bilayer, and thicker graphene on 300 nm SiO_2 is shown in Figure 1-6 [9].The contrast depends on number of layers of
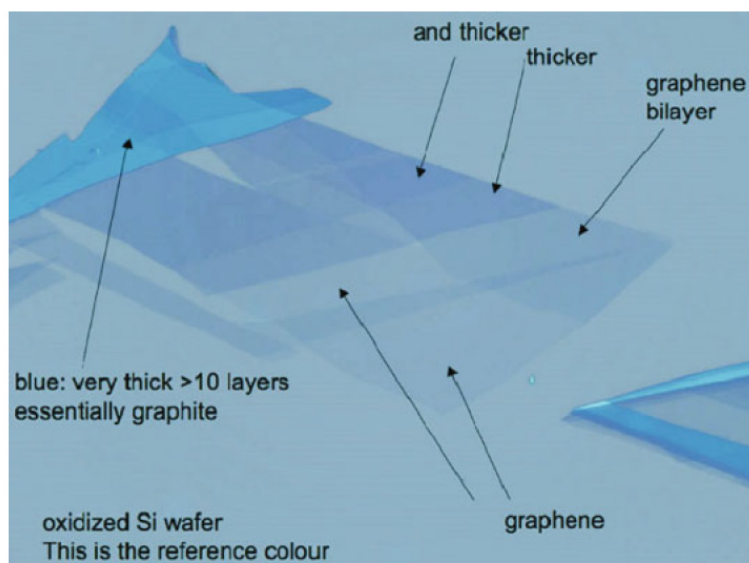
Figure 1-6   Optical image of graphene on 300 nm SiO_2, transferred by scotch tape. The optical contrast increases as the number of layers increase [9].

graphene, thickness of SiO_2, wavelength of light and illumination angle [9,17,18]. Blake et al. showed that graphene can be visualized on top of SiO_2 with any thickness except < 30 nm and around 150 nm, but the use of proper filter is required [17].

Electron microscopy

Scanning electron microscopy (SEM) has been used to study the dimensions of graphene grain boundaries and wrinkle formation in CVD synthesized graphene [19]. Monolayer graphene was transferred to transmission electron microscopy (TEM) grid and aberration-corrected annular dark-field scanning transmission electron microscopy (ADF-STEM) was used to visualize the stitching of grain boundaries in graphene synthesized via CVD, as shown in Figure 1-7 [20]. Cross-sectional transmission electron microscopy has been used numerous times to characterize the number of layers of graphene [21].
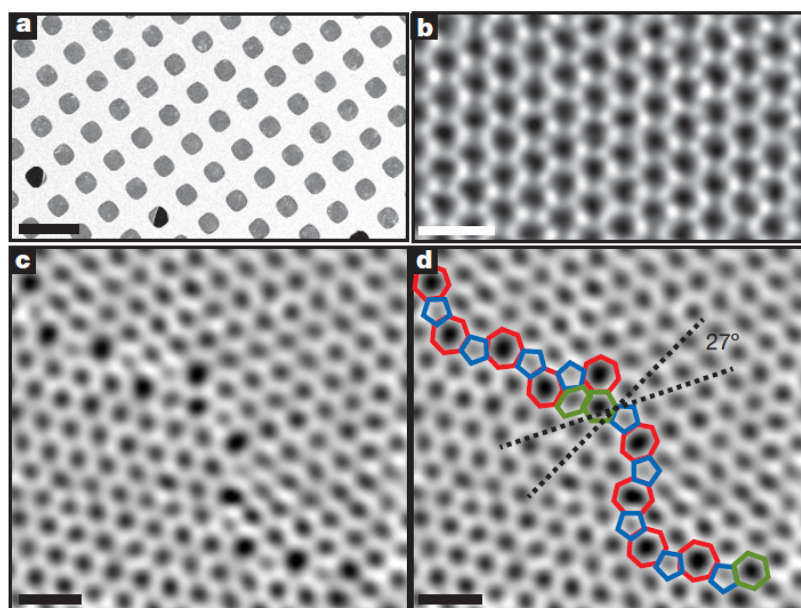
Figure 1-7   ADF-STEM images of graphene synthesized by CVD. (a) SEM microscope image of graphene transferred on transmission electron microscopy grid, (b) ADF-STEM image of graphene showing defect free hexagonal structure, (c) ADF-STEM image showing defects at grain boundary, (d) The two grains intersect at 27˚ relative rotation [20].

<u>Graphene synthesis</u>

Graphene can be synthesized through various routes e.g. mechanical exfoliation, chemical vapor deposition (CVD), epitaxial growth on silicon carbide, heating of solid carbon sources, etc.

Mechanical exfoliation

Mechanical exfoliation, also known as Scotch tape method, was the first reported method for graphene synthesis [3]. Although this method gives small size crystals, but synthesis and transfer of graphene flakes are extremely low-cost and convenient. The method requires peeling of graphene layers by adhesion provided by the scotch tape and then transferring the layers from the tape to a substrate. The number of layers transferred can be controlled to some extent by controlling the applied adhesive force and high quality crystals with insignificant atomic defects are obtained. Besides scotch tape method, ultrasonication of graphite dispersed in organic solvents and intercalation of graphite by sulphuric and nitric acids at high temperatures have also been reported [21].

Chemical vapor deposition

CVD involves the decomposition of hydrocarbons at high temperatures. Carbon from decomposed gasses gets adsorb on transition metal surfaces and synthesize graphene. Various transition metals have been used, but the synthesis on Ni and Cu has been studied widely.

Carbon has high solubility in Ni which makes it hard to control the number of layers of graphene on Ni. Moreover, grain boundaries due to polycrystalline nature and wrinkle formation are also the main problems to get high-quality and low-defect graphene. The evolution of graphene growth on Ni was studied by decomposing $^{12}CH_4$ and $^{13}CH_4$ on 700 nm evaporated Ni films. The Raman modes of ^{12}C and ^{13}C are at different frequencies and CH_4 from these two isotopes were flown sequentially. The Raman spectrum showed overlapping and uniformity in the distribution of ^{12}C and ^{13}C

over the whole surface, supporting the idea that growth is a combination of surface segregation and precipitation, as shown in Figure 1-8(a) [22].

CVD of large-area few-layers graphitic films on Ni sheets (10 × 10 mm) was reported in 2007 by Obraztsov et al. Gas mixture $H_2:CH_4 = 92:8$ under P = 80 Torr was decomposed at 950 °C to deposit graphitic films. The deposition time was varied from 5–10 min. The SEM images on Ni after growth showed smooth grains with size ~1 μm. Raman spectrum, scanning tunneling microscopy and Auger electron spectroscopy exhibited the deposited films had thickness 1.5±0.5 nm [23]. The effect of cooling rate after deposition to control the segregation of carbon on Ni was reported later. Commercially bought Ni foils were placed under $CH_4:H_2:Ar = 0.15:1:2$ with a total gas flow rate of 315 standard cubic centimeter per minute (sccm) at 1000 °C and pressure at 1 atm for 20 min. Samples were cooled down at different rates (20 °C/s, 10 °C/s and 0.1 °C/s). High resolution transmission electron microscopy depicted typically 3–4 layers thick graphene. Raman spectrum for sample cooled at ~10 °C/s showed smaller D peak intensity and I_{2D}/I_G ratio was ≤ 4. With slow cooling rate a more intense D peak is observed and I_{2D}/I_G was ≤ 1. As cooling rate increased to ~20 °C/s, no peak in the Raman spectrum was observed. It was thus suggested that the cooling rate significantly affected the thickness and defects of graphene films (with the medium cooling rate ~10 °C/s found to be ideal) [24].

Synthesis of few layer graphene on poly-nickel substrate with focus on wrinkle formation was studied by Chae et al. Highly-crystalline graphene was synthesized at high temperature (1000 °C) and low pressure (10^{-3} Torr). Optimum growth time (5 min) with $H_2:C_2H_2$ (45:2) mixture was reported. Wrinkle formation was studied and attributed to overlapping of adjacent flakes and difference in the thermal expansion of graphene layers with Ni substrate during cooling process [19].

Soon after, graphene (1-4 layers) was synthesized on evaporated Ni films by atmospheric pressure CVD and transferred to flexible and transparent substrate. The Ni

film was heated to 1000 °C and a gas mixture of CH$_4$:H$_2$:Ar (50:65:200 sccm) was used at atmospheric pressure. The sample was cooled at ~10 °C/s. The optimized Ni film thickness for better quality graphene was ~300 nm. After transfer to transparent substrate, 93% optical transmittance was achieved for reduced growth time. Moreover, the measured electron mobility of transferred graphene was ~3750 cm^2 V^{-1} s^{-1} [25].
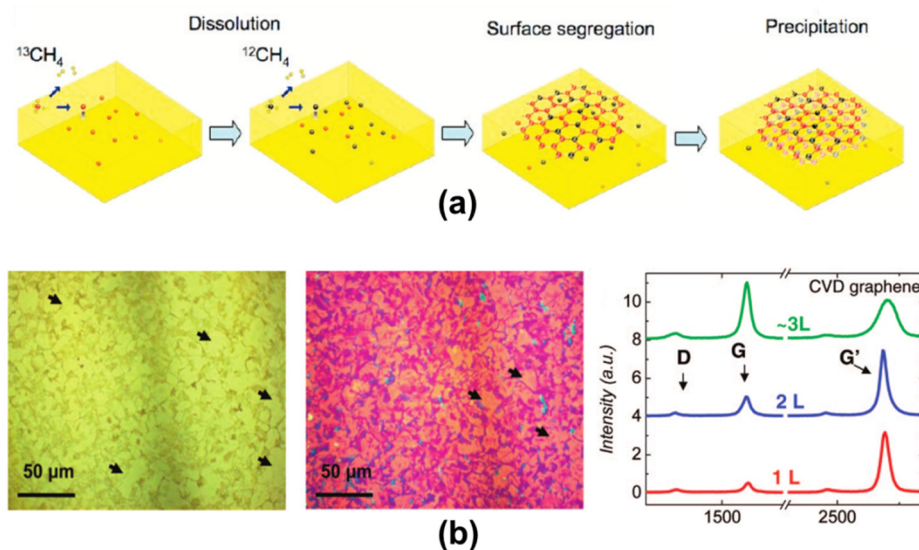
Figure 1-8   CVD of graphene on Ni. (a) The schematics of the evolution of graphene growth on Ni studies by isotope labeling. The growth is a combination of surface segregation and precipitation. [22], (b) Optical images of synthesized graphene on Ni by chemical vapor deposition and transferred to SiO$_2$. Raman spectra of graphene transferred to SiO$_2$ show synthesized monolayer, bilayer and three layer graphene [26].

Reina et al. reported the synthesis of few-layer graphene (1 to ~10 layers) on evaporated Ni films by atmospheric pressure CVD. Continuous films that were single-layer or few-layer formed over the entire Ni area and transferred to 300 nm SiO$_2$ as shown in Figure 1-8 (b). Carrier mobility ranging from 100 to 2000 cm^2 V^{-1} s^{-1} was measured and the lower value was attributed to grain boundary scattering and ineffective gate coupling [26]. Synthesis on Ni (300 nm) and Cu (700 nm) evaporated on 3 inch

diameter SiO$_2$ substrate was reported by decomposition on CH$_4$ at 1000 °C under atmospheric pressure. For ~5 minutes growth time, the number of graphene layers synthesized on Cu varied from 1-2, whereas, on Ni the number of layers ranged from 3-8 [27]. To reduce the defects at the grain boundaries single crystal nickel films has been used. Nickel (111) has been compared with polycrystalline nickel films and monolayer/bilayer coverage was reported on 91.3% of 60 × 50 μm^2 area as compared to 72.8% for later [28].

Carbon has low solubility in Cu and the synthesis is claimed to be surface limiting process rather than a combination of surface-segregation and precipitation [22]. Thus copper is more suitable for the synthesis of monolayer graphene. It has low melting point and de-wetting of copper at elevated temperature causes discontinuity and wrinkles in the graphene sheets [21]. Thus thick copper films are required for low defect graphene synthesis. Large-area single synthesis of single-crystal growth of graphene on 25 μm thick copper foil has been reported by decomposing CH$_4$ at 1000 ˚C under 500 mTorr. The electron mobility extracted from FET measurements was ~4000 cm^2 V^{-1} s^{-1} 29]. Roll-to-roll production of graphene up to 30-inch length on transfer and flexible substrates has also been demonstrated by CVD on Copper foil [30].

<div align="center">Applications of Graphene as Electrodes</div>

Owing to its excellent physical properties, several devices based on graphene have been reported. It has been used in field-effect transistors (FETs), flash and resistive memories, giant-magneto-resistance devices and so on [9,31-35]. Moreover, due to its high current density, thermal conductivity, mechanical strength, optical transmittance, flexibility and chemical stability, graphene is an ideal material to be used as electrodes in future electronic devices. The use of graphene as electrode in transistors, memory devices, solar cells and light emitting devices is the latest field of interest. A brief review of electronic devices using graphene as electrodes is given below.

The use of graphene as electrode in organic FETs, to decrease the contact resistance and enhance the hole-mobility has been reported in recent times. Di et al. used CVD graphene on Cu and Ag films as electrodes in a pentacene based FETs. Owing to high work function of Cu and Ag, there is a small hole-injection barrier in case of graphene-pentacene interface and hole-mobility in $0.47 - 0.53$ cm^2 V^{-1} s^{-1} range was reported [36].

The use of patterned grapheme electrodes by reduction of solution processed graphene oxide has also been reported in poly(3-hexylthiophene) (P3HT) based FETs. Linear behavior was observed at low voltages in the output characteristics of the device, suggesting the presence of ohmic contact between graphene and P3HT [37].

Transparent flexible electrodes based on monolayer graphene have been reported in pentacene FETs as shown in Figure 1-9. Carrier mobility of the device was 0.54 ± 0.04
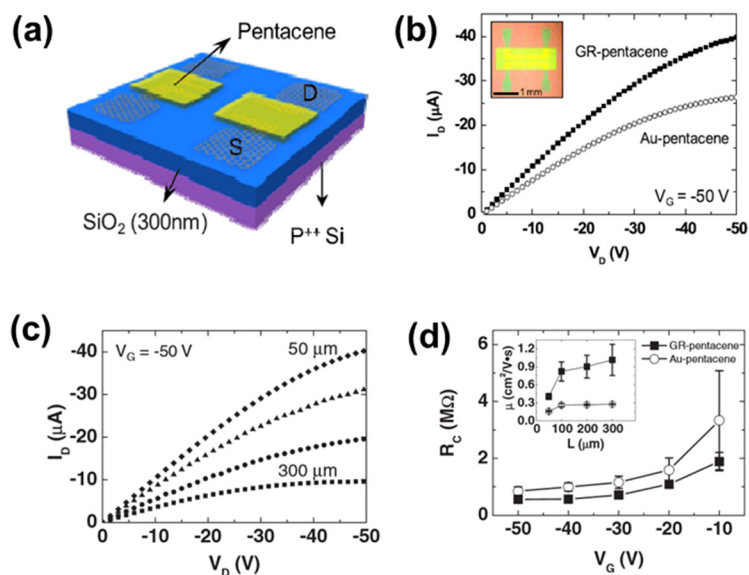
Figure 1-9   Pentacene transistor with graphene electrodes. (a) Schematics of the device, (b) comparison of device drain-characteristics with Au electrodes, (c) drain-characteristics with varying channel length, (d) comparison of contact resistance of transistor with graphene electrodes with Au electrodes at various gate voltages. [39].

cm^2 V^{-1} s^{-1}, as compared to the control samples with Au electrodes having mobility 0.02 cm^2 V^{-1} s^{-1} [38]. Recently, pentacene FETs with multilayer graphene electrodes have been compared with transistors having Au electrodes [39]. The device with channel lengths from 50 μm to 300 μm were fabricated and the contact resistance under various bias conditions was measured as shown in Figure 1-9 (c,d). A lower contact resistance was achieved in case of graphene electrode based device, despite the fact that hole-barrier height at graphene-pentacene interface is more than at Au-pentacene interface. This was attributed to the formation of favorable interfacial dipole layer at the graphene-pentacene interface, thus reducing the actual hole-barrier height.

The use of graphene as electrodes in memory devices has also been reported. Lee et al. used multilayer graphene electrodes in resistive switching memory based on Pr$_{0.7}$Ca$_{0.3}$MnO$_3$ (PCMO). The device (MLG/PCMO/Pt) showed rewritable switching and it was attributed to the functionalization of multilayer graphene by the movements of ions from PCMO [40]. The use of monolayer graphene electrodes with ability to store charge has also been reported in a flexible and transparent non-volatile memory based on carbon nanotubes field-effect transistor. Graphene transferred to polyethylene terephthalate (PET) surface (transparent and flexible), was used as source, drain and gate electrodes. The device schematics with important characteristics are shown in Figure 1-10. The exposure to ozone resulted in the formation of C–O–C, C–O and C–OH bonds that acted as charge traps. The device also showed good optical transmittance owing to high optical transmittance of graphene (absorbing only 3.6 % of light). A memory window of ~10 V was achieved when gate voltage was scanned in ±10 V range. The on-off current ratio of the device was ~2 × 10^2. The memory showed fast switching in the range of 100 ns, due to the traps in graphene. Mechanical bending test with edges at ~8 mm radius showed good endurance for 1000 cycles [41].
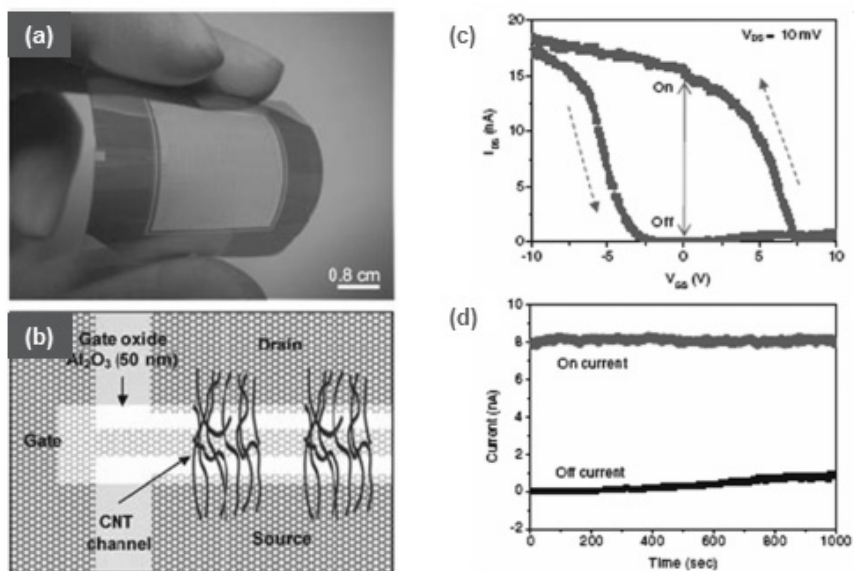
Figure 1-10   Flexible, transparent non-volatile memories based with graphene electrodes. (a) Device image showing flexibility, (b) schematics of the device showing CNT channel with graphene as source, drain and gate electrodes, (c) Transfer characteristics of the device showing ~10 V memory window, (d) Endurance characteristics of the device under mechanical bending [41].

Graphene has also been used as electrodes in a polyimide:6-phenyl-C61 butyric acid methyl ester (PI:PCBM) composite based memory, showing write-once read-many (WORM) behavior. Earlier, the same material showed rewriteable switching with metallic electrodes. The devices were fabricated on flexible substrate and displayed stable transport characteristics under bending condition as shown in Figure 1-11(a,b). The ON current remained stable under harsh bending conditions and showed good endurance after various bending cycles as shown in Figure 1-11(c,d) [42].

Moreover, the use of graphene as electrodes in touch screen, liquid crystal displays, light-emitting diodes and solar cells is a current research interest and has been reported frequently in recent times [43].
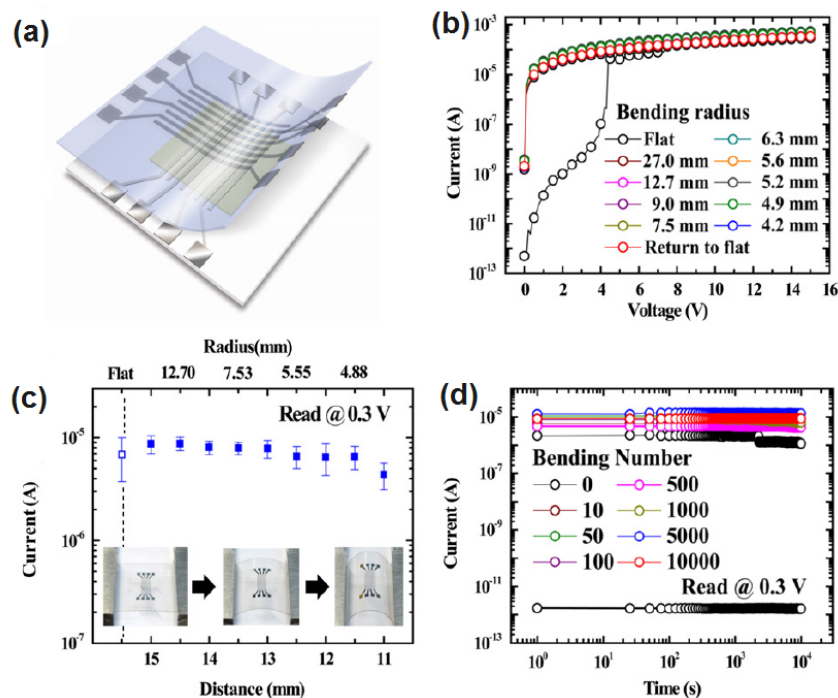
Figure 1-11   Flexible memory based on multilayer graphene electrodes (a) Device schematics, (b) Transport characteristics of the device under various bending conditions, (c) Variation in the device current under various bending conditions, (d) Retention characteristics under various bending conditions [42].

In this chapter, a review on the physical properties, characterization and synthesis of graphene has been highlighted. Moreover, the uses of graphene as electrodes in recent reports have also been discussed. The organization of the rest of the thesis is as follows. Chapter 2 focuses on the synthesis and characterization of bilayer graphene by atmospheric pressure CVD with ultra-fast cooling method. Chapter 3 reports the synthesis of pyrolytic carbon and explains a method to accurately measure the in-plane crystal size. In chapter 4, graphene membranes have been used as electrodes in a molecular memory and a stable operation resulting from atomically-smooth covering is discussed. Chapter 5 summarizes the findings of the thesis and discusses the future directions to carry on this work.

CHAPTER 2

SYNTHESIS OF BILAYER GRAPHENE ON NICKEL

Introduction

Monolayer and bilayer graphene are semi-metals with zero bandgap. However, bandgap is a fundamental requirement for semiconducting applications. Various techniques have been reported to induce bandgap in graphene e.g. patterning graphene into nanoribbons, adding dopant impurities and substrate effect [44-49]. In addition to these techniques, bilayer graphene inherently induces bandgap due to symmetry breaking, thus making it an important material for semiconducting applications [9,10,32,50-52].

The first experimental observation of bandgap induction in bilayer graphene was reported by Ohta et al. as shown in Figure 2-1 [53]. Bilayer graphene was synthesized on
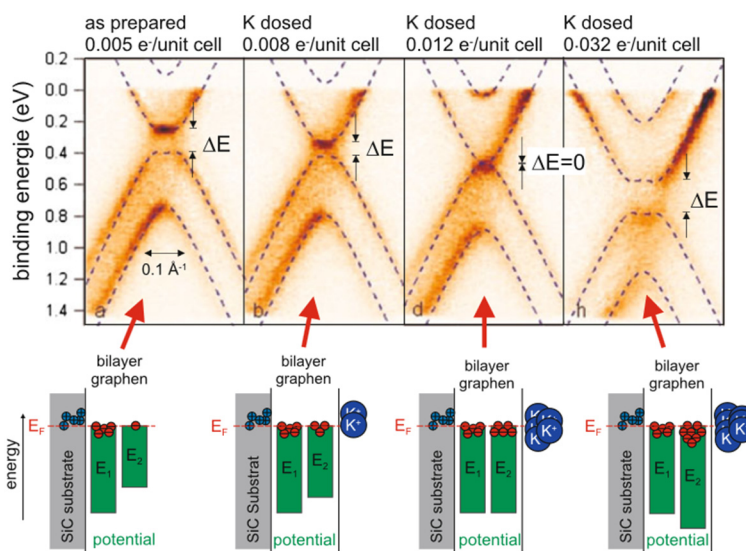
Figure 2-1   Closing and opening of the band gap in bilayer graphene induced by potassium adsorption on top of the bilayer stack. Doping reduces the difference between the on-site potentials. For $E_1 = E_2$, the gap is closed. Further potassium dosing increases the potential difference again ($E_1 > E_2$), which results in bandgap reopening [9].

SiC and angle-resolved photoemission spectroscopy (ARPES) was used to measure the electronic propertie. The symmetry of the bilayer graphene was broken by accumulation of charges on the graphene layer next to SiC interface due to depletion layer created in the SiC [9,53]. Thus two graphene layers were different in terms of charge and electrostatic potential, and a bandgap was observed at K-points. Alkali metal doping was carried out to donate electrons to the upper layer of bilayer graphene, to rearrange the symmetry. With appropriate doping the bandgap was closed and regenerated as can be observed in Figure 2-1.

Gate-induced bandgap in the bilayer graphene was reported later. A double gated structure was fabricated to simultaneously control the Fermi level and electric field perpendicular to the graphene layer, as shown in Figure 2-2 (a) [54]. The square resistance of bilayer graphene as a function of back-gate and top-gate voltages are shown in Figure 2-2 (b,c), respectively. It was clearly observed that the resistance of the device increases when top-gate and bottom-gate have opposite polarities, suggesting the bandgap induction is due to the symmetry breaking.

Due to bandgap generation and gate-controlled conduction in the bilayer graphene, scalable synthesis of defect-free bilayer would be the first step towards the realization of semiconducting bilayer graphene devices. Graphene synthesis on transition metals by CVD or via segregation of solid carbon sources is generally a scalable process [19,25,27,55,56]. As discussed in Chapter 1, Ni and Cu have generally been used as substrates for graphene growth. Several hydrocarbons, like methane (CH_4), acetylene, ethylene, propane, etc. have been decomposed in atmospheric and low pressure CVD [21]. Besides the CVD of the above mentioned gases, C_{60} and solid polymers such as poly(methyl metha-crylate), polystyrene and acrylonitrile butadiene styrene have also been decomposed to grow graphene [57-59].
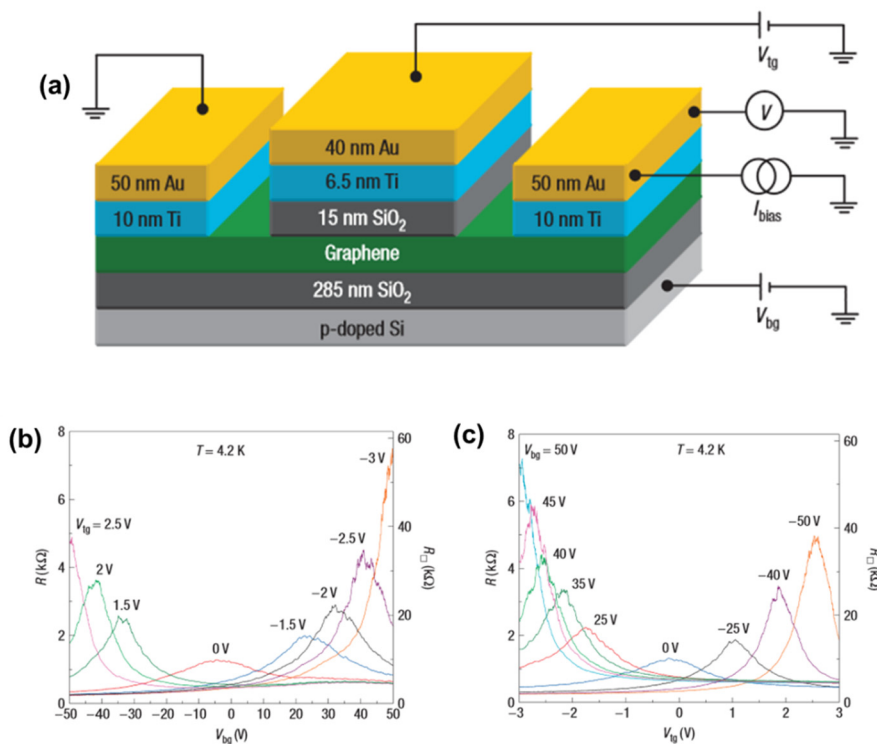
Figure 2-2   Double-gate device to control the bandgap and Fermi level of bilayer graphene. (a) Schematic of the double-gate device, (b) Resistance versus back-gate measured for fixed values of top-gate voltages at 4.2 K. The height of the resistance peak shows the opening of the bandgap under opposite voltage at top- and bottom-gates, (c) Resistance versus top-gate for fixed values of back-gate voltages. The behavior is similar to (b) and resistance peak increases when applied voltages at two gates are opposite [54].

Graphene synthesizes on Ni due to combination of surface segregation and precipitation of carbon at high temperatures. As carbon has high solubility in Ni, the precipitation of extra carbon occurs at the Ni surface during cooling. Since the precipitation is a non-equilibrium process, this makes thickness control of graphene a challenge [21]. Precipitation of carbon can also be controlled by controlling the cooling rate [24,56,60-62]. Very high cooling rate has been reported to deposit amorphous carbon deposition, whereas low cooling rate leads to no growth [24]. Moreover, segregation of extra carbon to deposit thin graphene films can be controlled by reducing Ni film

thickness. It has been reported that the carbon segregation on Ni is non-uniform at low temperatures. However, CH_4 has high decomposition temperature, which helps in constant carbon coverage over the Ni surfaces [63]. Furthermore, high melting point of Ni enables high temperature annealing, which results in larger domains, and thus making it favorable for large area low defect growth [21].

In this chapter, a method to control the precipitation of extra carbon on Ni surface during the cooling-down process is reported, thus synthesizing uniform bilayer graphene. The sample temperature is reduced from the growth temperature of 1000˚C to a temperature closer to room temperature in a few seconds which leads to a uniform bilayer graphene growth.

Chemical Vapor Deposition Synthesis of Bilayer Graphene

Bilayer graphene was grown on a 300 nm Ni film, evaporated on SiO_2 (300 nm)/Si substrate. Si/ SiO_2 substrate was treated with 10 minutes acetone, 10 minutes methanol, 10 minutes DI rinse, 20 minutes nanostrip (commercial Piranha substitute), followed by another 10 minutes DI rinse. After cleaning, Ni was evaporated by using e-beam evaporator at 1 Å/s, under $<1 \times 10^{-7}$ Torr. $Ni/SiO_2/Si$ samples were gently cleaned in UV ozone for 2 minutes, before loading in to the CVD furnace. UV ozone eliminates organic contaminants from the Ni film, which is important for defect free growth. Process gases were supplied by Airgas with research grade 5.0 (minimum purity 99.999%). The samples were loaded into the CVD furnace (Lindbergh/Blue, 1 inch tube diameter) at room temperature and heated to 700˚C in 200 sccm Ar ambient. At 700˚C, 65 sccm H_2 was introduced in addition to the Ar. The temperature was ramped to 1000˚C in Ar:H_2 ambient. To stabilize the growth temperature, the samples were further annealed for 10 minutes, after reaching 1000˚C. Ar:H_2 annealing sequence leads to increased grain size and decreased surface roughness [55,56]. Finally, H_2 was turned off and bilayer graphene was synthesized by introducing CH_4 into the furnace, in addition to the already flowing

Ar gas. A wide process parameters were explored and bilayer graphene was obtained by; (a) varying the growth time (50, 60, 120 s) under a constant CH_4 flow-rate (23 sccm); (b) varying the flow rates (6, 12, 23 sccm) under a constant growth time (120 s). After the growth, the sample temperature was reduced within few seconds by pulling the quartz tube out of the hot region of the furnace. Process diagram showing the furnace temperature and gasses along with their flow rates are shown in Figure 2-3.
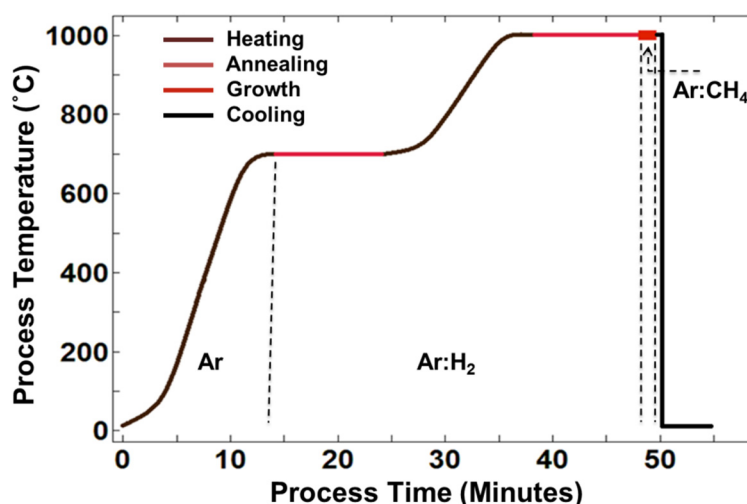
Figure 2-3   Process diagram showing different stages during the CVD of grapheme on Ni. Note: The temperature of samples from 1000 – 0 °C during the ultra-fast cooling is approximation and just to give the idea.

For material characterization, Raman spectroscopy (Raman Nicolet Almega XR Spectrometer) was used in the point scan and the area scan mode. A 532 nm laser (10 mW power) was used with a 0.6 μm spot size, 15 seconds scan time and 4 scans per point. To examine the uniformity of the synthesized graphene, the I_{2D}/I_G ratio was taken over an area of 200 μm × 200 μm. In each pixel of the area scan, 2.1 μm spot size was used with 15 s scan time, 4 scans per pixel and 10 μm step size.

Characterization of Bilayer Graphene

The growth time was first varied to study the effect on the number of layers, uniformity and defect density of the synthesized graphene. Raman spectra in random point scan mode along with the optical images of the samples with growth times 50, 60 and 120 seconds under 23 sccm CH_4 are shown in Figures 2-4, -5 and -6, respectively. The I_{2D}/I_G ratio is close to unity for these growth times, which confirms the synthesis of bilayer graphene.
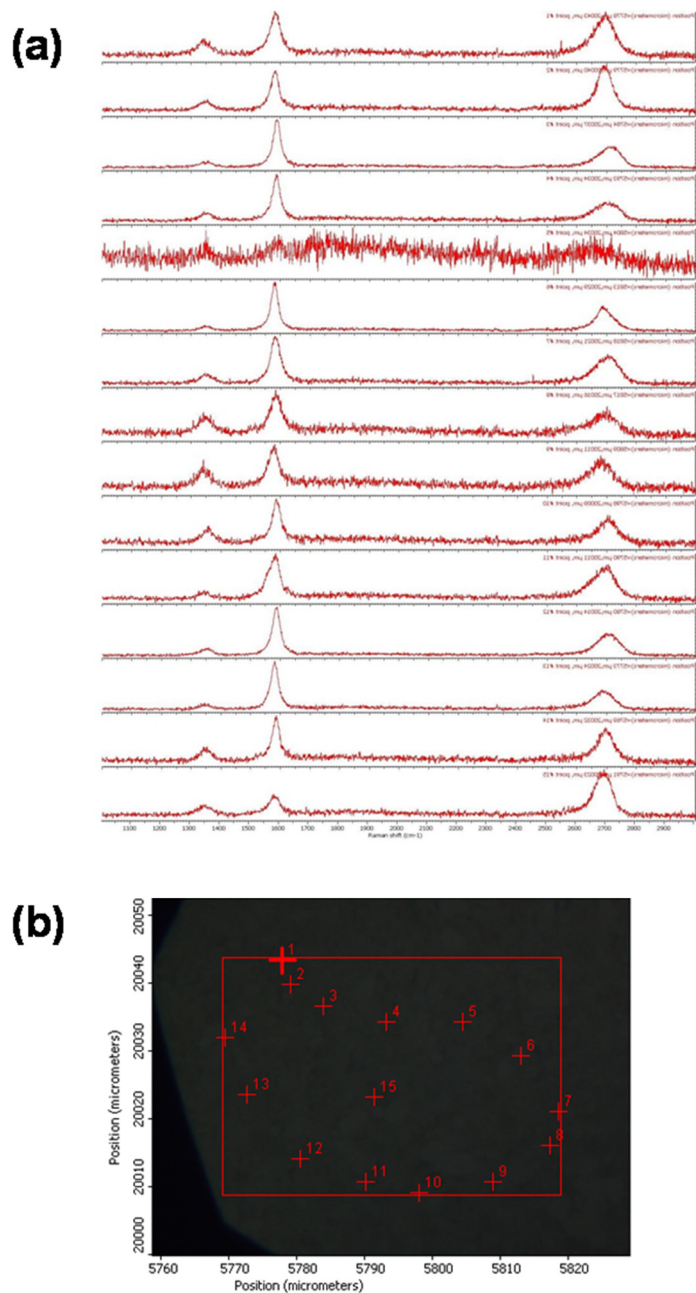
Figure 2-4   Raman spectra in random point scan mode for the sample treated with 23 sccm CH_4 for 50 seconds. (a) Raman spectra at random points on the sample. The I_{2D}/I_G ratio is around 1 with large D peak intensity, (b) Optical image of the sample showing the points where the spectrum is taken.

Figure 2-5   Raman spectra in random point scan mode for the sample treated with 23 sccm CH_4 for 60 seconds. (a) Raman spectra at random points on the sample. The I_{2D}/I_G ratio is around 1 with noticeable D peak intensity, (b) Optical image of the sample showing the points where the spectrum is taken.
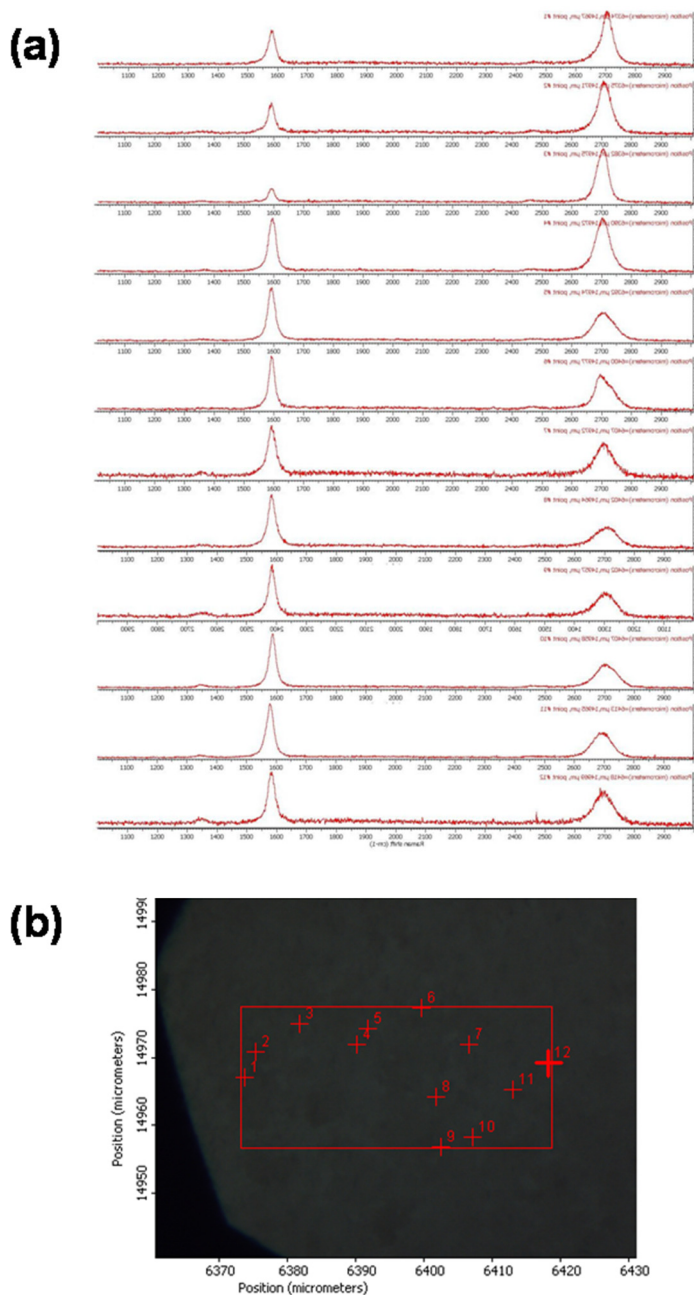
Figure 2-6   Raman spectra in random point scan mode for the sample treated with 23 sccm CH_4 for 120 seconds. (a) Raman spectra at random points on the sample. The I_{2D}/I_G ratio is around 1 with negligible D peak intensity, (b) Optical image of the sample showing the points where the spectrum is taken.

The number of layers of synthesized graphene are uniform and it is due to the quenching of the samples along with the tube, as reduced Ni temperature inhibits the precipitation of carbon on Ni surface. Furthermore, after turning the CH_4 off if there is some residual carbon inside the furnace the fast cooling suppresses its further segregation. By comparing the Raman spectra of these three processes as shown in Figure 2-7, it is observed that the intensity of the D peak decreases, as the growth time increases from 50 to 120 s. The I_D/I_G ratio is taken over 20 random locations, for each sample. The mean and standard deviation of I_D/I_G are plotted in an error bar graph shown Figure 2-8. The average I_D/I_G ratio for the sample grown under 23 sccm CH_4 for 120 s is 0.1, with a standard deviation of 0.05, which suggests a low defect density of bilayer graphene for these parameters.
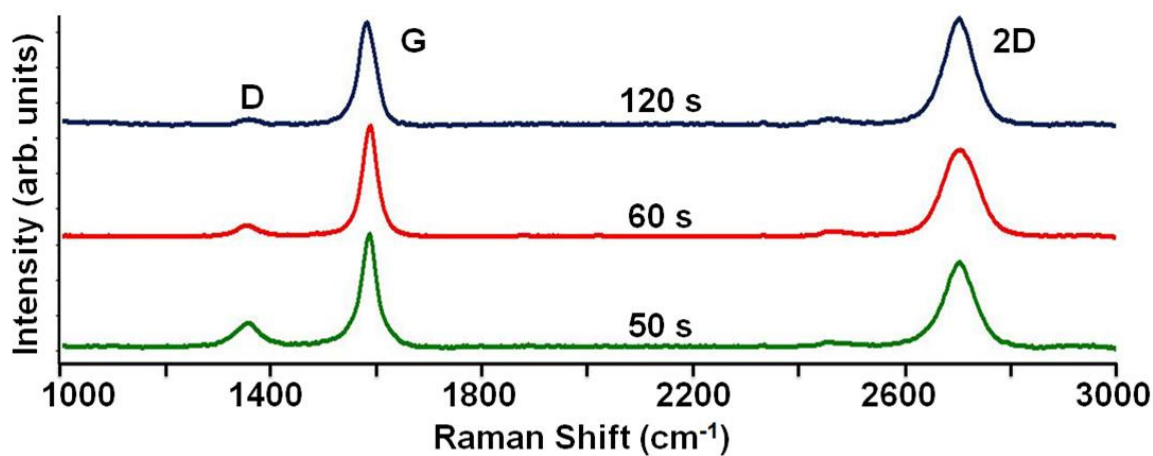
Figure 2-7   Raman spectra for various growth times. Increasing the growth time decreases the D peak intensity for 23 sccm of CH_4.
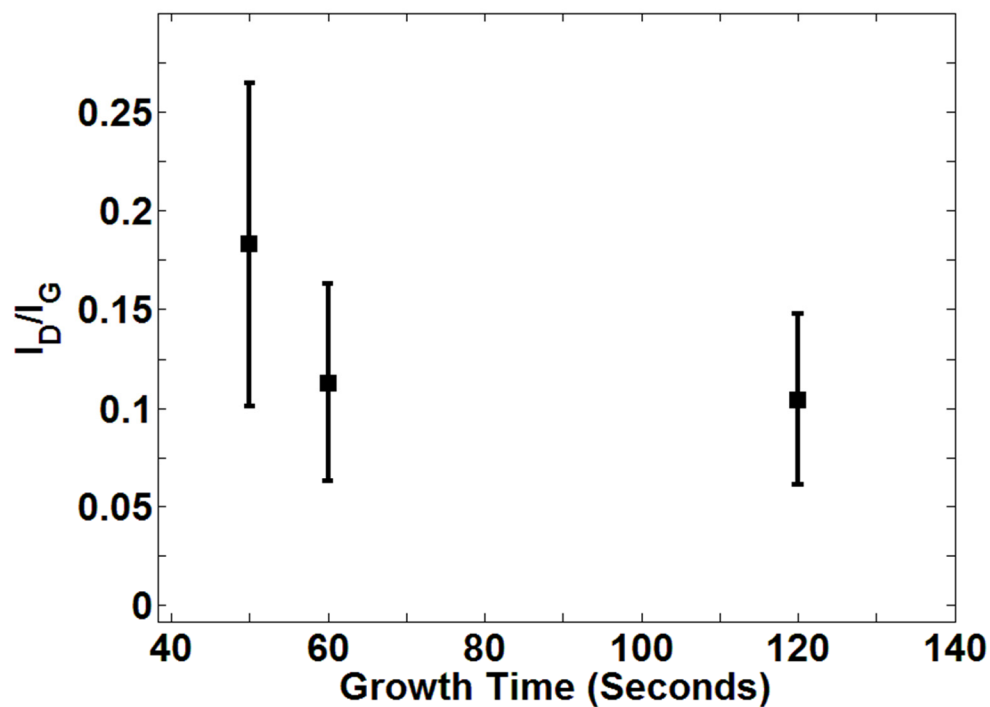
Figure 2-8 I_D/I_G ratio for various growth times. The average defect density decreases with increasing growth time.

Afterwards, the effect of the CH_4 flow rate on the synthesis was studied. Raman spectra of random point scan along with the optical images of the samples with growth time 120 s under 23, 12 and 6 sccm CH_4 are shown in Figures 2-6, -9 and -10, respectively. It shows the bilayer graphene growth is consistent for a wide range of flow rates.
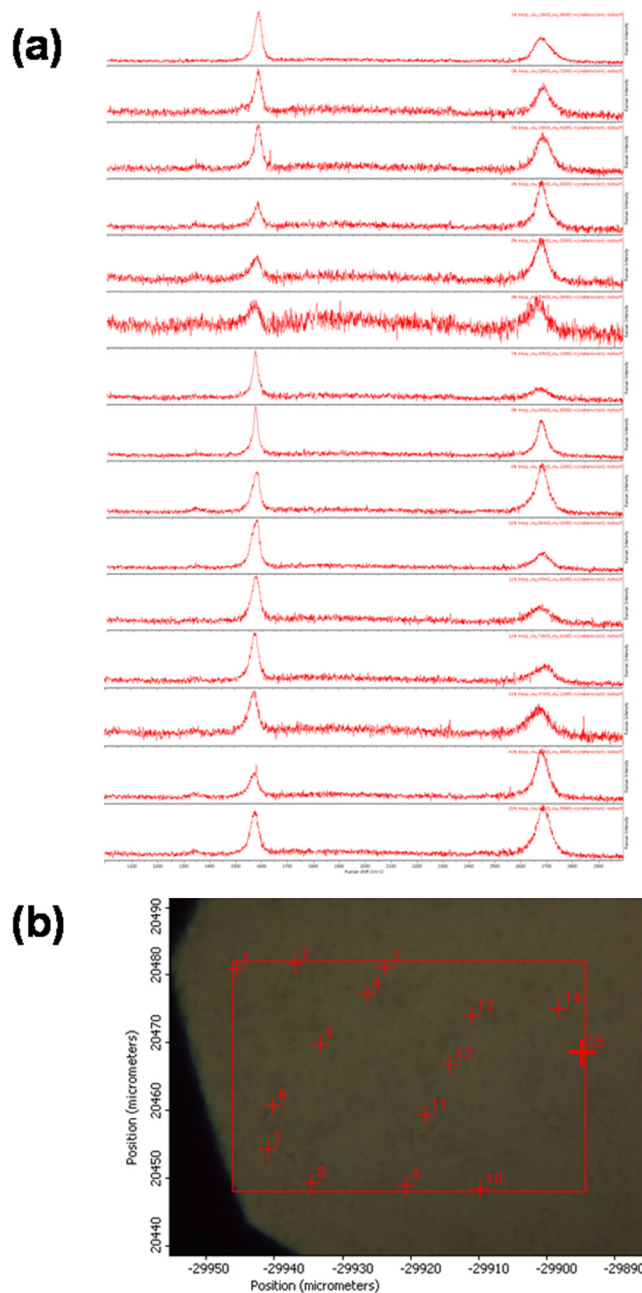
Figure 2-9   Raman spectra in random point scan mode for the sample treated with 12 sccm CH$_4$ for 120 seconds. (a) Raman spectra at random points on the sample. The I$_{2D}$/I$_G$ ratio is around 1 with negligible D peak intensity, (b) Optical image of the sample showing the points where the spectrum is taken.
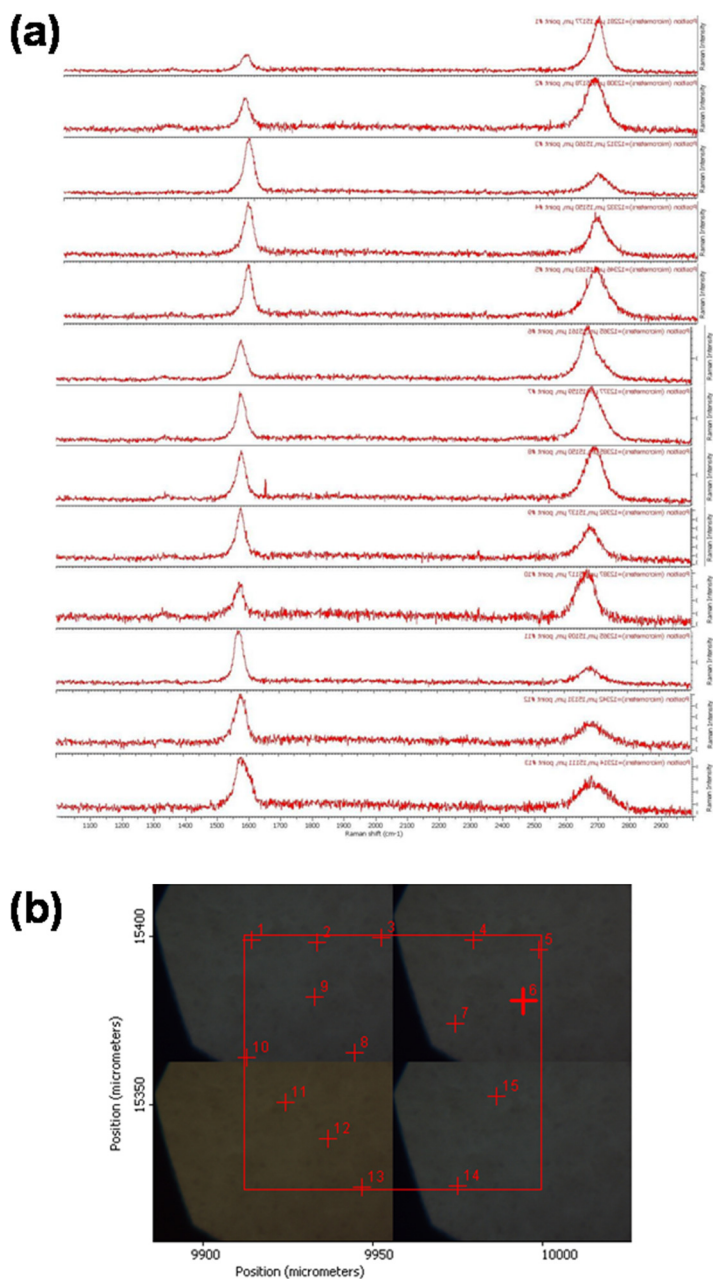
Figure 2-10   Raman spectra in random point scan mode for the sample treated with 6 sccm CH_4 for 120 seconds. (a) The I_{2D}/I_G ratio is around 1 with negligible D peak intensity, (b) Optical image of the sample showing the points where the spectrum is taken.

By comparing the Raman spectra of these three processes as shown in Figure 2-11, it is observed that the defect density of bilayer graphene is small for the samples grown under wide CH_4 flow rates for 120 s.
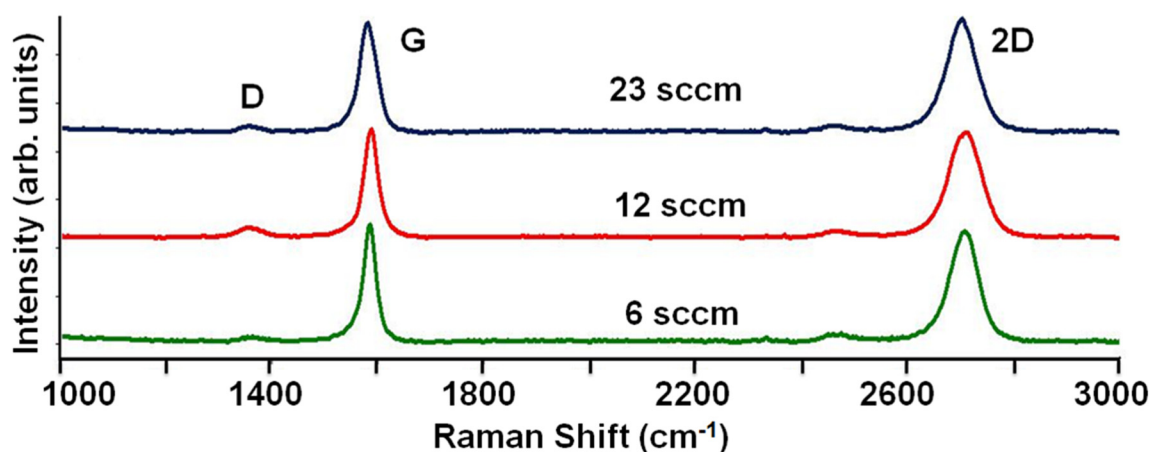
Figure 2-11   Raman spectra for various CH_4 flow rates. The D peak intensity is less for 120 seconds growth time under varying flow rates.

To measure the uniformity of the synthesized graphene over large area, Raman area maps are taken on the sample treated with 23 sccm of CH_4 for 120 s. Figure 2-12(a,d) show the I_{2D}/I_G ratio at two different locations. In each case, the I_{2D}/I_G ratio is in the range of 0.9 to 1.6 over 96 percent of the total 200 μm × 200μm area. This suggests that the bilayer graphene is grown over a larger percentage of area on polycrystalline Ni film [12,56,64,65]. The I_{2D} and I_G plots over these locations are shown in Figures 2-12(b,e) and 12(c,f) respectively. These plots show a uniform intensity distribution for the G and D peaks which further implies the graphene sample uniformity.

Quenching the samples from hot region of the furnace helps in reducing the non-equilibrium precipitation of extra carbon on the Ni surfaces during the cooling process and the main growth mechanism is diffusion of carbon on Ni surface due to the
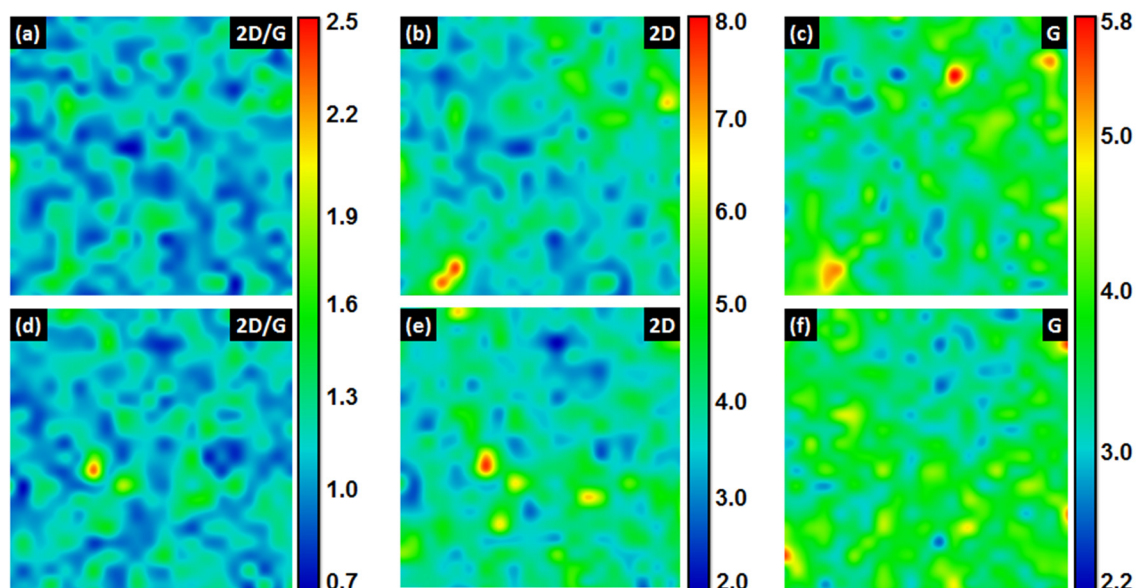
Figure 2-12   Two-dimensional Raman intensity map for bilayer graphene. (a) I_{2D}/I_G ratio (ratio of 2D to G peak intensities). (b) I_{2D} (intensity of 2D peak). (c) I_G (intensity of G peak). (d), (e) and (f) show I_{2D}/I_G, I_{2D} and I_G, respectively, for a different area. Bilayer graphene was grown by using CVD on 300 nm of evaporated Ni film under CH_4/Ar (23:200 sccm) at 1,000°C for 120 s. The total area of each view map is 200 μm × 200 μm.

decomposed CH_4. With fast cooling, the reduced samples temperature stops further segregation of carbon due to any residual carbon inside the furnace, even after CH_4 flow is turned off. The thickness of the graphene is almost constant even with a wide range of CH_4 flow rates (6 to 23 sccm), which shows that the segregation process is rather self-limiting. Furthermore, the growth temperature is high due to high decomposition temperature of CH_4 that supports the uniform carbon diffusion over the Ni surface. This helps in growing uniform and less defect density bilayer graphene. Moreover, as the growth time is decreased, the average intensity of the D peak increases with indicates incomplete growth. This further verifies the self-limiting equilibrium segregation of carbon on Ni surface, with reduced out-diffused carbon atoms from the C-Ni solution due to fast cooling. To verify the proposed growth mechanism, graphene was grown on 300

nm Ni films, with 23 sccm CH_4 flow rated for 120 s, with cooling the samples within the furnace. Due to slow cooling, the precipitation of carbon on Ni surface from C-Ni solution is a dominant process, which leads to non-uniform graphene growth.

Yet another way to reduce the precipitation of extra carbon is to reduce the thickness of Ni film, as thin Ni films would absorb less carbon and thus contribute to further decrease in out-diffused carbon. To characterize this effect, the growth was performed on 100 nm and 200 nm thick Ni films, with 23 sccm CH_4 flown for 120 s. The Raman spectra of the synthesized graphene along with the optical images are shown in Figure 2-13. For 200 nm, the I_{2D}/I_G ratio is close to unity and the area uniformity is similar to 300 nm thick films. However, growth on 100 nm Ni film results in increased surface roughness. Although the I_{2D}/I_G ratio is still around unity in this process, but surface coverage is only 50 percent.

In conclusion, a new method to synthesize bilayer graphene through CVD of CH_4 on polycrystalline Ni films with an ultra-fast cooling technique has been reported. The number of layers of graphene is uniform over a wide area with low defect density. The growth is consistent over a certain variation of CH_4 flow rate and growth time.

CHAPTER 3

SYNTHESIS AND CHARACTAERIZATION OF PYROLYTIC CARBON

Introduction

Pyrolytic carbon is an important nanomaterial due to its high chemical stability, and good electrical and thermal conductivities [66]. It has been used as thin electrodes in dynamic random access memories, metal-insulator-semiconductor capacitors, and electrochemical sensing applications [67-69]. It has also been employed as interlayer material in solid oxide fuel cells and biomedical applications [70,71]. Pyrolytic carbon is usually synthesized by the decomposition of hydrocarbons and their subsequent deposition on catalyst substrates.

In early reports of pyrolytic carbon synthesis, Lucas and Marchand studied the effect of temperature (1030 – 1092 °C), pressure (150 – 400 mm Hg) and flow rate of methane (2.1 – 6.3 liter/h) on the synthesis of pyrolytic carbon on silica and carbon felt. Thin pyrolytic carbon layers were deposited on silica as compared with felt. Polarized light microscope showed a strong optical anisotropy and the deposited material was rough laminar. It was further showed that the carbon deposition increased with temperature and pressure, while at constant temperature and pressure, deposition decreased with flow rate decrease. The growth mechanism was attributed to the decomposition of CH_4 into benzene and other hydrocarbons like acetylene, pyrene and flouranthene. The benzene gets deposited on the substrate to synthesize pyrolytic carbon [72]. Pyrolytic carbon with different anisotropies was synthesized by varying temperature and pressure of propene. As the temperature was increased (800 to 1200 °C) and/or the partial pressure of propene was decreased, the textures varied from smooth laminar – rough laminar – isotropic. X-ray studies was done and revealed the presence of small amorphous carbon peak along with sp^2-hybridized carbon peak. The effect of pressure on

the texture of pyrolytic carbon was studied by Hu et al. by measuring the orientation angle from selected area electron diffraction [73]. Increasing methane pressure improved the texture up to intermediate value, and at the higher value of pressure the texture degree decreased again. The synthesis was regarded as a two-step process. First pyrolytic aromatic hydrocarbon as parts or elements of graphene layers was formed and then condensation of graphene layers was resulted due to condensation of aromatic hydrocarbons on the substrate. Recently, synthesis of thin conducting pyrolytic carbon films on SiO_2 by decomposition of methane was reported. Thickness and roughness of the films were controlled by varying the pressure, temperature and deposition time. The films had low resistivity $\sim 2 \times 10^{-5}$ Ωm and high optical transmittance $\sim 93\%$. High resolution electron microscopy depicted the texture was laminar with domain sizes $\sim$ 2nm [66].

<u>In-Plane Crystal Size</u>

Besides anisotropy of pyrolytic carbon, another important material parameter for carbon based nanomaterials is the in-plane crystal size (L_a), which can be determined by I_D/I_G ratio in the Raman spectrum [74,75]. For pyrolytic carbon, there are additional bands which overlap with the D and G bands, thus making it complex to determine L_a. A general method to measure L_a of pyrolytic carbon is reported in this Chapter. The D and G bands are first extracted from the original Raman spectrum and then the peak intensities of these bands are used in a laser excitation energy dependent equation to calculate L_a. Furthermore, by taking the Raman area map over 100 μm $\times$ 100 μm area, the mean value and the standard deviation of L_a over the entire area has also been reported. The pyrolytic carbon film characterized has been synthesized by decomposing methane on a 300 nm evaporated Ni film at 1000 ˚C in a CVD furnace. Ni is being used due to high solubility of carbon in it, which leads to a small growth time. Moreover, the

precipitation of extra carbon on Ni surface can also be controlled by the ultra-fast substrate cooling method during CVD [76].

Synthesis of Pyrolytic Carbon

Si/SiO$_2$(300 nm) was first cleaned with 10 minutes acetone, 10 minutes methanol, 10 minutes deionized (DI) water rinse, 20 minutes nanostrip (commercial Piranha substitute), followed by another 10 minutes DI water rinse and nitrogen dry. Subsequently, 300 nm Ni was evaporated by using electron beam evaporator (Angstrom Engineering) in an alumina crucible. The evaporation rate was 1 Å/s, and the chamber pressure was $< 10^{-7}$ Torr. UV ozone cleaner was used to clean the Ni surface, before loading it in the CVD furnace. This helps in eliminating organic contaminants, which is important for the purity of synthesized pyrolytic carbon film. Research grade 5.0 (minimum purity 99.999%) process gases were used, which were supplied by Airgas. The sample was loaded into CVD furnace (Lindbergh/Blue, 1 inch tube diameter) at room temperature and heated to 700˚C in 200 sccm (standard cubic centimeter per minute) Ar ambient. At 700˚C, 65 sccm H$_2$ was introduced in addition to the Ar and the sample was annealed for 10 minutes. The temperature was then ramped to 1000˚C in the Ar:H$_2$ ambient. To stabilize the growth temperature, the sample was annealed for 10 more minutes after reaching the 1000˚C ambient temperature. Finally, H$_2$ was turned off and the pyrolytic carbon was synthesized by introducing 23 sccm CH$_4$ into the furnace for 40 s, in addition to the already flowing Ar gas. The sample temperature was then suddenly reduced by pulling the quartz tube out of the hot region of the furnace within a few seconds.

Raman spectroscopy (Raman Nicolet Almega XR Spectrometer) in the point scan and the area scan mode was used to characterize the synthesized pyrolytic carbon films. 532 nm laser (10 mW power), with a 0.6 μm spot size, 15 seconds scan time with 4 scans per point was used in the point scan mode. To examine the uniformity of the synthesized

pyrolytic carbon, I_D/I_G ratio was measured over an area of 100 μm × 100 μm in the area scan mode. In each pixel of the scanned area, a 2.1 μm spot size was used with 15 s scan time, 4 scans per pixel and 5 μm step size.

<center>Characterization of L_a of Pyrolytic Carbon</center>

Figure 3-1(a) shows the Raman spectrum of the synthesized pyrolytic carbon film in the point scan mode. The two significant peaks are centered at ~1354 and ~1584 cm^{-1} with the non-zero intensity between these wavenumbers. Moreover, the 2D
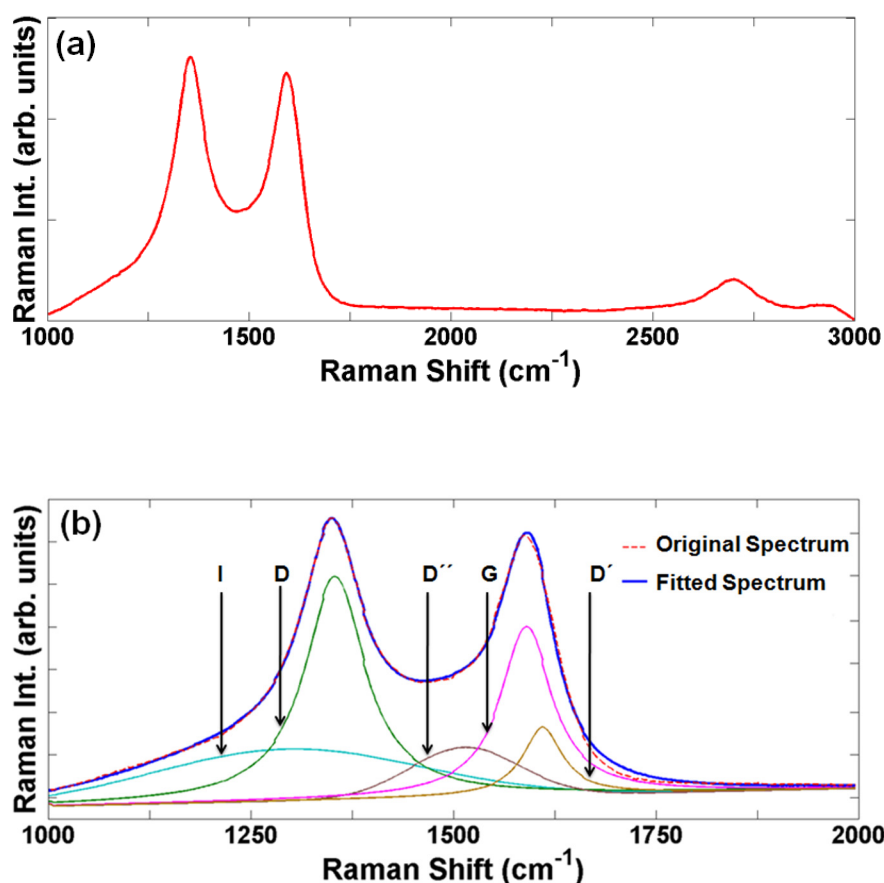
Figure 3-1   Raman spectrum in the point scan mode. (a) Raman spectrum of pyrolytic carbon film, (b) Deconvolution of various bands in the low wavenumber range, showing the D, G, D′, D″ and I bands. Dashed line is the fitted spectrum. Various bands with their respective extracted parameters are reported in Table 3-1.

band is much broader and has smaller intensity. These characteristics in the Raman spectrum confirm the synthesis of pyrolytic carbon [66,77]. The Raman spectrum in the low wave-number range can be further de-convoluted as shown in Figure 3-1(b). Besides the regular D and G bands, D′, D″ and I bands can be fitted to get the deconvoluted spectrum. Lorentzian functions are used for fitting the D, G and D′ bands, while Gaussian functions are used for fitting the D″ and I bands. The extracted parameters i.e. the peak center, the peak intensity and the full-width at the half-maximum are reported in Table 3-1. The G band is the first order Raman process due to in-plane vibrations of C-C atoms [9,11-13]. The D and D′ bands are the intra and inter-valley Raman processes due to the defects in the sp^2 hybridized carbons, respectively [11,12,78]. The D″ and I bands are considered to originate from the amorphous carbon and the sp^2-sp^3 bond combinations respectively [79,80].

Table 3-1   Parameters of various deconvoluted bands.

Band	Fit Type	Band Center (cm⁻	FWHM (cm⁻¹)
I	Gaussianan	1295.00	387.33
D	Lorentzian	1353.99	89.64
D″	Gaussian	1513.76	159.43
G	Lorentzian	1584.00	75.52
D′	Lorentzian	1610.00	57.85

The Raman intensity area maps for the peaks at ~1354 cm⁻¹ and ~1584 cm⁻¹ wavenumbers are shown in Figure 3-2(a,b), respectively. The Raman spectrum at each point is deconvolved and the G and D bands are extracted. The area maps of the extracted D and G peak intensities (I_D, I_G) are shown in Figure 3-2(c,d), respectively. The ratio of
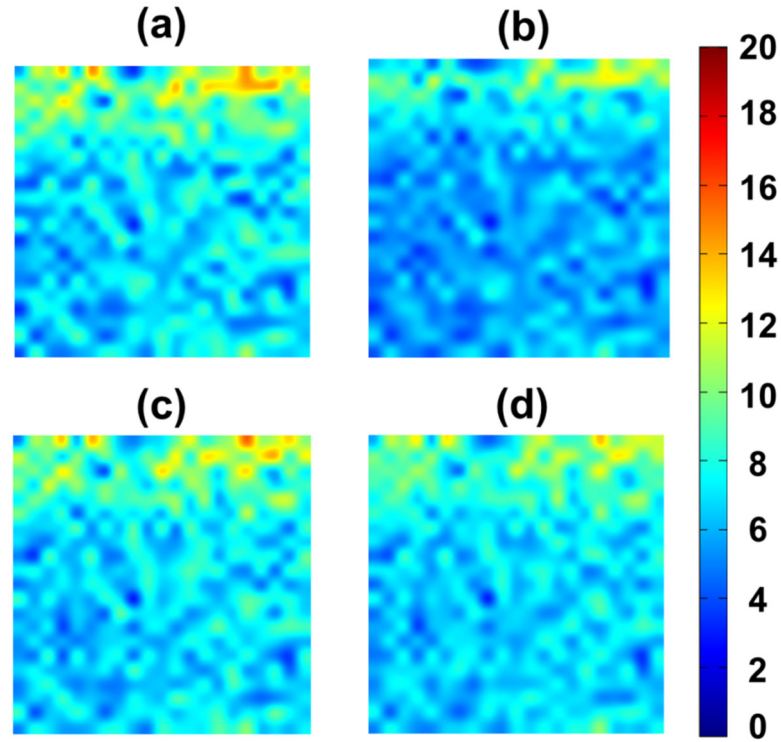
Figure 3-2   Two-dimensional Raman intensity maps. The peaks in the original spectrum are observed at, (a) ~1354 cm^{-1} and (b) ~1584 cm^{-1} wavenumbers. The intensity maps of the extracted (c) D peak and (d) G peak from the deconvoluted spectra. The pixel size is 5 μm × 5 μm with the scanned area of 100 μm × 100 μm.

D to G peak intensities was plotted by using the extracted D and G peaks, as shown in Figure 3-3. By using this ratio and the energy or wavelength of the excitation laser, L$_a$ for pyrolytic carbon is given as [9,75]:

$$L_a(nm) = \frac{560}{E_{laser}{}^4}\left[\frac{I_D}{I_G}\right]^{-1} = 2.4 \times 10^{-10}\, \lambda_{laser}^4 \left[\frac{I_D}{I_G}\right]^{-1}$$

where E$_{laser}$ and λ$_{laser}$ are the laser excitation energy (in eV) and wavelength (in nm), respectively. For a wavelength of 532 nm used in this study, the pre-factor is 19.2. In this context, commonly used value of 4.4 as the pre-factor [74] may not be valid in general. Using the above equation and putting I$_D$/I$_G$ ratio as shown in Figure 3-6, the mean value

of L_a over the scanned area is about 22.9 nm, with a standard deviation of 2.4 nm. This uniformity in L_a is due to the ultra-fast cooling of the sample – a method that also has also been used for bilayer graphene synthesis [76]. Although a detailed understanding is yet to be developed, such a cooling method seems to control the segregation of carbon on Ni surface rather well, enhancing the film uniformity.
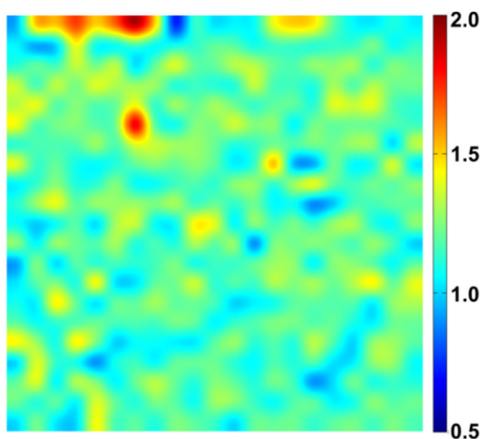
Figure 3-3   Two-dimensional plot of extracted I_D/I_G ratio of Raman spectra. The pixel size is 5 μm × 5 μm with the scanned area of 100 μm × 100 μm.

In summary, a method to calculate L_a of pyrolytic carbon films by using Raman spectroscopy has been elucidated. After extracting the D and G bands by deconvolving the original Raman spectrum, their peak intensities are used in a laser excitation energy dependent equation to calculate the L_a. From the Raman area map taken over 100 μm × 100 μm area, the L_a statistics has been reported– namely the mean value and the standard deviation. The synthesized pyrolytic carbon film has small standard deviation in L_a, due to ultra-fast substrate cooling. Furthermore, this method to calculate L_a can be used for any other carbon nanomaterial, in which additional bands overlap the D and G bands.

CHAPTER 4

MOLECULAR MEMORY BASED ON CARBON NANOMATERIALS

Introduction

Two terminal memories have been anticipated to replace the conventional non-volatile memories, due to their simple fabrication, low cost, high endurance, and low power consumption [81-83]. Compared to the three terminal memories, the structure of the two terminal memories are much simpler, possessing a switching material sandwiched between the two metal electrodes. Furthermore, the read/write architecture of the two terminal memories consists of the simple cross-bar metal electrodes, as compared to complex integrated circuit assembly of solid-state drives [84-86]. The device is either in the high-resistance state, or in the low-resistance state, depending on the conductivity of the sandwiched material. The two main classifications of the two terminal memories that depend on the reproducibility of I-V characteristics are: read-write-erase-rewritable memory and write-once-read-many (WORM) memory [87]. WORM memories have gained recent attention due to their potential use in the radio frequency identification tags, smart cards, data depositories and permanent data storage [88]. WORM memories with different switching materials e.g. hybrid organic/inorganic mixture, metal nanoparticles capped with surrounding conjugate compounds, fullerene mixed with aromatic polymers, graphene oxide and so on has been demonstrated [81,82,89-91]. The switching mechanism has been attributed to the filament formation, electromigration, thermal activation etc. [81-91].

Although filament formation and electromigration has been used as a source of switching in bistable memory devices, but numerous efforts have also been spent on diminishing this effect in electronic devices. In studying the novel nanomaterials, the change in conductivity due to the filament formation may be mixed with the material switching, causing ambiguities in predicting the conductivity of novel material. Thus,

reliable and efficient contacts are therefore an important aspect of device design at the nanoscale. Historically, the contacts in the micron-scale devices have only been part of the overall device design for minimizing the contact resistance based on Schottky barrier height [92-94]. At the nanoscale, however, the influence of contacts on the transport channel is so important that an equal or often times even more effort is spent on the contact and interface design [95,96]. In various nanoscale devices, the contacts even dominate the transport characteristics [97,98]. While various novel contacts exist at the nanoscale with unique density of states, the simplest ones are the Ohmic contacts used to inject and extract the charge carriers. Mostly metals have been used as such contacts. However, in addition to the atomic roughness and grain boundaries, such contacts suffer from electromigration or filament formation, which may deteriorate the device characteristics and lead to reliability issues [99]. One of the grand challenges thus for the nanoscale design is to provide smooth and reliable contact to nanomaterials, being free from electromigration and any other non-ideal effects. In this chapter, the objective is to explore graphene nanomembranes as a candidate for such contacts [9,100]. The use of graphene and boron nitride has been explored earlier for ultrathin circuitry [101].

<div align="center">Graphene Contacts to Inhibit Electromigration</div>

In this chapter, a two-terminal memory with bilayer graphene as an atomically-smooth contact has been fabricated. Although various device structures based on graphene have already been explored [33], but this structure is unique in the context of its use to improve reliability. The device schematic of the memory with bilayer graphene contact is shown in Figure 4-1(a). Bilayer graphene was synthesized on a 300 nm evaporated Ni film by CVD. This layer prevents the electromigration of Ni atoms into the active material of the device. Furthermore, the use of bilayer graphene instead of monolayer or several-layer graphene is twofold. As compared to the monolayer, the probability of complete coverage with bilayer graphene is higher in the presence of

defects and secondly, with increasing the number of layers, the transport properties of the device may be dominated by the multilayer graphene itself. Thus, bilayer graphene tends to provide an optimum solution. After bilayer graphene synthesis, a 100 nm C_{60} film was thermally evaporated, followed by the evaporation of 5 nm Silicon dioxide (SiO_2) by electron-beam. SiO_2 film serves as the protective layer for the subsequent high-temperature metal evaporation. Finally, 90 nm thick top Cr electrode was deposited by using a shadow mask in an electron-beam evaporator. A control sample without bilayer graphene was also fabricated to investigate the effect of graphene, as shown in Figure 4-1(b).

<p style="text-align:center"><u>Device Fabrication</u></p>

Bilayer graphene was synthesized on a 300 nm Ni film deposited on a 300 nm thermally grown oxide on Si substrate, using the recipe stated in Chapter 2. After bilayer graphene growth, 100 nm C_{60} film was deposited by using thermal evaporator (Edwards Coating System E306A) at 1Å/s rate under $< 7 \times 10^{-7}$ Torr chamber pressure. The commercial C_{60} powder was supplied by M.E.R Corporation. Raman spectroscopy was used to confirm the quality of evaporated C_{60}. Laser power of 2 mW with 5 s scan time and 4 scans per point was used to avoid sample heating. Next, the sample was loaded in the electron-beam evaporator, and 5 nm SiO_2 was evaporated, followed by 90 nm of Cr by using a shadow mask. The evaporation rates of SiO_2 and Cr were 0.2 Å/s and 1 Å/s, respectively, and the chamber pressure was $< 1 \times 10^{-7}$ Torr.

For the transport characterization, a pulse ramp with 10 ms ON time and 50 mV step voltage was applied by using Keithley 236 source-measure units. For endurance characteristics, a 0.4 V pulse with 10 ms duration and 0.1% duty cycle was applied.

A detailed characterization of the synthesized bilayer graphene has been reported Chapter 2. The Raman spectrum of evaporated C_{60} film on bilayer graphene is shown in Figure 4-1(c). The dominant peaks are at 491 cm^{-1}, 1464 cm^{-1} and 1596 cm^{-1}

wavenumbers, which confirms the coherence of C_{60} molecular structure even after thermal evaporation [102,103].
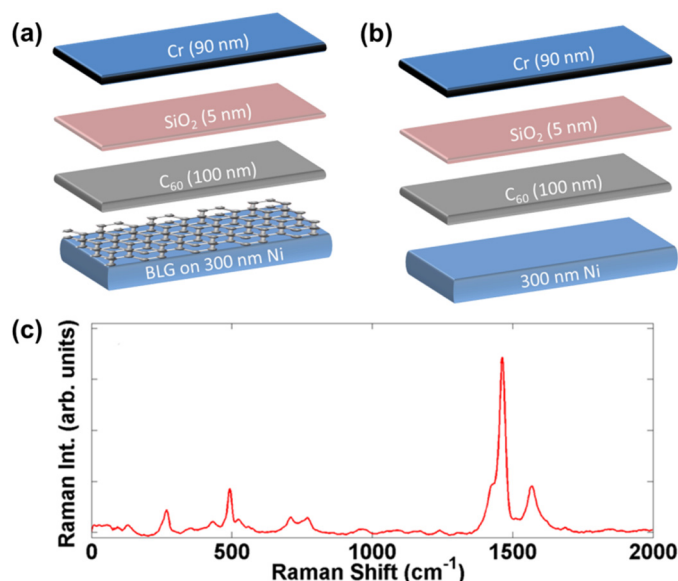
Figure 4-1   Device schematics and characterization. (a) Molecular memory with atomically-smooth bilayer graphene sandwiched between 300 nm Ni and 100 nm C_{60} films, (b) Control device without the bilayer graphene, (c) Raman spectrum of evaporated C_{60} film on the bilayer graphene.

<u>Electrical Characterization</u>

In Figure 4-2, the transport characteristics in the first and second sweep cycles for the device with BLG contact are shown. The device starts in the low-resistance state and the voltage is increased in the forward direction till it irreversibly switches to high resistance state at about 0.9 V, as shown in Figure 4-2(a). After switching, the device withstands its high-resistance state, thus exhibiting hysteresis in the remaining cycle. We rule out the possibility of conductive filament formation (CFF) due to electromigration, since graphene has a breaking strength value of ~42 N/m and is impermeable even to helium atoms [7,8]. Moreover, in the CFF, current increases after switching, whereas opposite behavior is observed here. Apart from this, we find that the switching voltages

for various devices lie in the $0.8 - 1.2$ V bias range. This variation may be due to the amorphous and heterogeneous nature of the evaporated SiO_2 film [104].
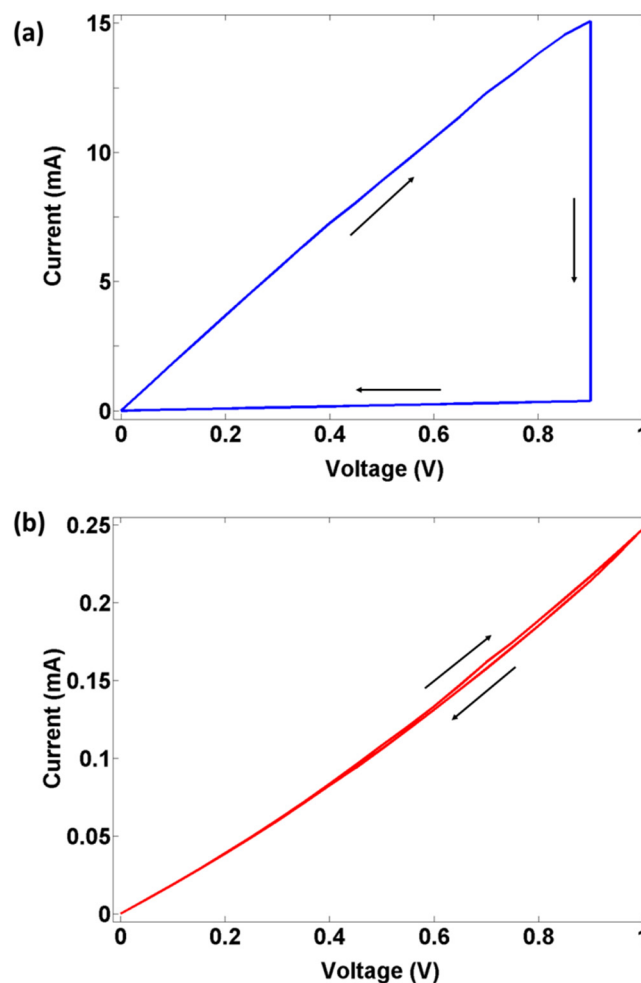
Figure 4-2   Transport characteristics in first and second sweep cycles. (a) During the first sweep cycle, the voltage is swept in the forward direction till it switches to high-resistance state. During the reverse sweep, the device remains in the high-resistance, and shows hysteresis. (b) The device remains in the high- resistance state during the second sweep cycle and no hysteresis or switching is observed.

The switching behavior for the second sweep cycle is shown in Figure 4-2(b). The device remains in the high-resistance state without any hysteresis behavior. In the

subsequent sweep cycles, the device sustains its high-resistance state, thus making it a WORM memory.
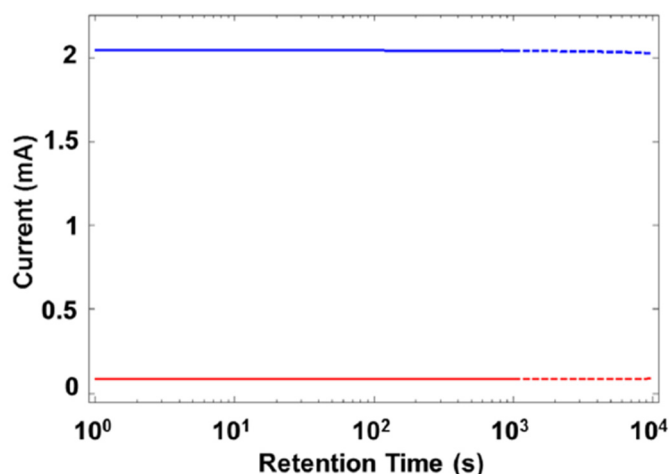
Figure 4-3   Retention characteristics. The memory device shows a stable low-resistance state with a 0.4 V read voltage pulse of 10 ms duration for 10^3 s. After switching to the high-resistance state by applying a 1.05 V write pulse of 10 ms duration, stable current is observed again. The dashed line is the interpolation to 10^4 s.

The retention characteristics of the device are shown in Figure 4-3. The device is read by using a voltage pulse train of 0.4 V bias with 10 ms duration and 0.1% duty cycle. The mean value of current in the low-resistance state is 2.041 mA with a standard deviation of 0.973×10^{-3}. The device is then switched to the high-resistance state by applying a program voltage pulse of 1.2 V bias with 10 ms duration. The mean value of current is 89.29 μA with the standard deviation of 0.155. The current ratio of low-resistance to high-resistance state in this device is about 22.85 (which varied in 20-40 range for various devices). Besides the high retention time, the device also shows good endurance when continuous reading cycles with small pulse duration is applied. The

retention characteristics are extrapolated to 10^4 s, and a stable behavior is foreseen in both states of the device.

In Figure 4-4, the transport characteristics of the control sample without the bilayer graphene contact are shown. The device shows random switching and irreproducible hysteresis. It is observed that the current in this device is much higher as compared to the one with the bilayer graphene contact. Moreover, the current variation from device to device in the control sample is also considerable. This irregular behavior in the control sample may be due to the atomically rough interface between Ni and C_{60}, as well as the electromigration of Ni atoms across C_{60}/Ni interface.
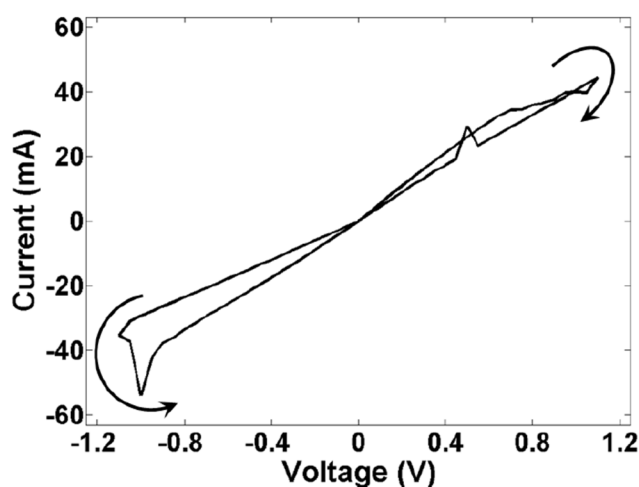
Figure 4-4   Transport characteristics of the control device without the bilayer graphene. The voltage is first swept in the positive cycle, then by a negative sweep cycle. A random switching with irreproducible hysteresis is observed.

The switching mechanism in the reported WORM memory device with the bilayer graphene contact is not clearly understood yet, but covering Ni film with bilayer graphene prevents the electromigration of Ni atoms into C_{60} film, thus stabilizing the

device behavior. The transport characteristics do not show ohmic or space-charge-limited conduction. Similar devices using C_{60} molecules have been reported to have rewritable switching characteristics - quite different observation from this device [82, 015]. Moreover, multilayer graphene electrodes used in devices with PI:PCBM composite as active material have also been recently reported to have WORM memory behavior, whereas with the metallic electrodes rewritable switching characteristics has been reported [42]. Although the channel materials are different in the two experiments, the connection between the use of graphene and WORM features is noteworthy and needs to be explored further. Carbon nanotube based contact have also been explored to eliminate electromigration [106], however, we believe graphene nanomembrane provides a better interface due to its 2D nature.

In conclusion, a molecular memory device with atomically-smooth bilayer graphene contacts has been fabricated. Covering Ni film with bilayer graphene shields the channel from metal surface irregularities and also prevents the electromigration of Ni atoms into the C_{60} film. The device switches from a low-resistance to a high-resistance state, followed by hysteresis in the first sweep cycle. In the subsequent sweep cycles, the device remains in the high-resistance state and no hysteresis is observed, thus showing WORM memory behavior. The switching voltages vary in $0.8 - 1.2$ V bias range for various devices with the high-resistance to low-resistance ratio vary in 20-40 range. The retention characteristics show good endurance under both low-resistance and high-resistance states up to 10^4 s.

CHAPTER 5

OUTLOOK

In this work, a method to synthesize uniform and low-defect bilayer graphene by atmospheric pressure CVD on Ni films has been established. Graphene synthesis on Ni is a combination of surface segregation and precipitation, which makes uniform growth a challenge. Ultra-fast cooling was employed to control the precipitation of extra carbon on Ni surface, thus resulting in uniformity of synthesized graphene. Raman spectroscopy revealed that the bilayer graphene was grown over a wide range of CH_4 flow rates and growth times. Therefore, the method is also reliable under small fluctuations related to equipment [72].

Furthermore, synthesis of pyrolytic carbon and determination of its L_a by using Raman spectroscopy was reported. Pyrolytic carbon was synthesized by CVD on Ni films. Due to high solubility of carbon in Ni, this leaded to small growth time, as compared to the growth time on typically used SiO_2. Furthermore, a method to calculate the L_a by using Raman spectroscopy was elucidated. The Raman spectrum was deconvolved in the low-wavenumber region and G and D bands were extracted to calculate the L_a by using a commonly acknowledged equation. This technique would provide further validation in the characterization of pyrolytic carbon films along with transmission electron microscopy and polarized light microscope [107].

Moreover, a molecular memory with atomically-smooth bilayer graphene contacts was fabricated. Graphene was used as a contact due to its high conductivity, high breaking strength and impermeability. Graphene provided WORM memory behavior and stopped the electromigration of Ni atoms into the active material of the device. The devices showed good retention and endurance characteristics. The control devices showed irregular switching and hysteresis, due to electromigration of Ni atoms into C_{60}.

Thus graphene not only provided WORM behavior, but also served to improve the reliability of device [108].

We envision the use of ultra-smooth graphene contacts for nanoscale devices and organic electronics, providing reliable and efficient operation without electromigration. Moreover, graphene, pyrolytic carbon and C_{60} also have potential to be used as charge storage nodes in memory devices. Flash memories based on Si with C_{60} as charge storage nodes have been reported to have good memory window and retention characteristics [109]. Flash memories based on either pyrolytic carbon, graphene, or C_{60} as storage nodes with carbon nanotube as channel are expected to give more control over the conduction due to minimal percolation paths and high electric field resulting from 1D nature of channel. A schematics of such a device with C_{60} as storage node is shown in Figure 5-1.
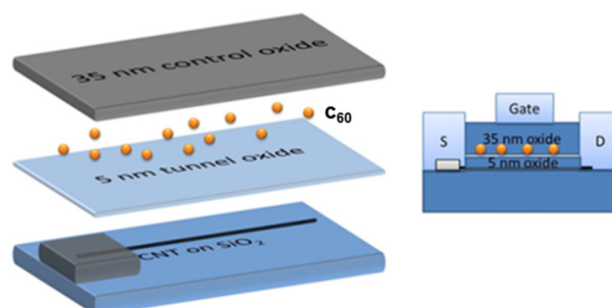
Figure 5-1   CNT flash memory with C_{60} as charge storage nodes.

APPENDIX A

RAMAN SPECTROSCOPY OF GRAPHENE RELATED SYSTEMS

Different techniques have been used to characterize graphene related systems. The physical morphology has been acquired by using electron microscopy [20,21], but it may be destructive to the sample. Atomic force microscopy has been used to characterize the number of layers of graphene [21,26], but the interlayer distance between graphene sheets is close to its working limit and the technique is also time consuming. Optical microscopy of graphene on SiO_2 was the first method to visualize graphene [17,81], but it is not accurate for consistent characterization. Raman spectroscopy has been historically used to characterize the carbon allotropes and is a non-destructive technique. Since the discovery of graphene, it is the most widely used technique for its characterization. Different features e.g. defect density, number of layers, doping, strain etc. can be determined from Raman spectrum.

Introduction to Raman Spectroscopy

The scattering of light from a material depends on its electrical and vibrational properties. Thus, it can be used to characterize different materials having unique properties. If the scattered light has the same energy (wavelength or frequency) as the incident light, the process is elastic and is called Rayleigh scattering. On the contrary, if scattered light has different energy, the process is inelastic and is called Raman scattering [9,11]. When the energy of the scattered light is smaller (greater) than the incident light, quantized excitation has been created (annihilated) and the process is called Stokes (anti-Stokes) process, as shown in Figure A-1. Raman spectrum is a plot between intensity and frequency of the scattered photon.

As can be seen from Figure A-1, the energy of the system is conserved in a Raman process. Moreover, momentum of the system should also be conserved. The light used in a Raman scattering process is typically visible or near infrared. In this range, the
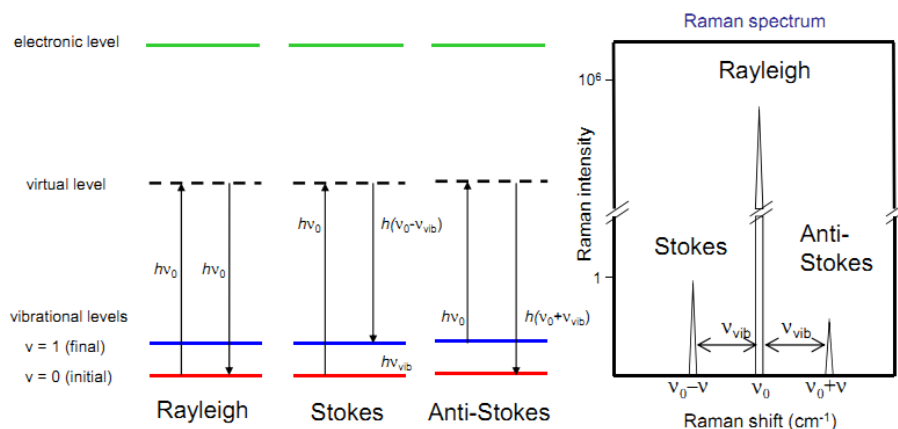
Figure A-1   Schematics of the Raman spectrum. (a) Elastic (Rayleight) and inelastic (Raman) scattering of photons, (b) Raman spectrum is a plot between scattered photon intensity and frequency.

wavevector of light is much smaller than the Brillouin zone boundaries. Thus quantum excitation has almost zero momentum, which corresponds to nearly vertical transition in the electron energy dispersion.

The order of the Raman scattering is the number of scattering events involved a Raman process. Thus for the first-order process, due to momentum conservation requirement, phonons with q ~0 would be allowed. In a higher-order Raman process, the photo-excited electron at stake k can be scattered to k + q and can go back to its original position at k after the second scattering event by a phonon with a wavevector –q. Thus the two phonons have their wavevector in opposite direction i.e. q + (–q) → 0, and the momentum is conserved. A quantum description of first and second-order Raman scattering processes is shown in Figure A-2 [11].
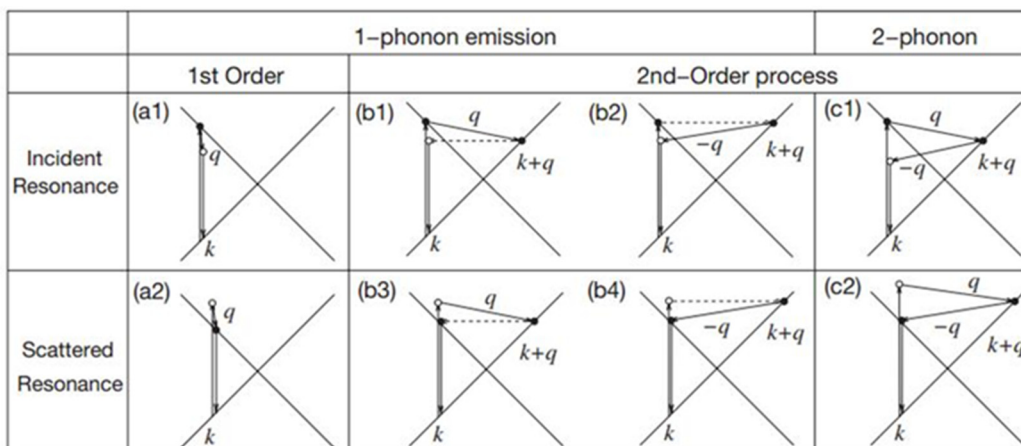
Figure A-2   Order of Raman scattering. (a1) One-phonon first-order, (b1) One-phonon second-order, and (c1) two-phonon second-order incident resonance Raman processes. (a2), (b2), (c2) are scattered resonance with the same order and phonon-emission. [11]

<u>Raman Spectroscopy of Graphene</u>

Understanding the phonon dispersion of graphene is important to understand the Raman spectrum. As graphene has two carbon atoms per unit cell, thus six branches in phonon dispersion relation are obtained as shown in Figure A-3. Three of the six phonon modes are acoustic (A) and the other three are optic (O) phonon modes. For the three acoustic and three optic phonon modes, one is an out-of-plane (oT) phonon mode and the other two are in-plane modes, one longitudinal (L) and the other one transverse (iTO). As a result, starting from the highest energy at the G point, the six phonon dispersion curves are assigned to LO, iTO, oTO, LA, iTA, and oTA phonon modes. Group theory tells us that the degenerate LO and iTO phonon mode (E_{2g} symmetry) are Raman active, while the oTO phonon mode is infrared active [11]. The Raman active modes give rise to different peak in the spectrum, as discussed in the following sections.
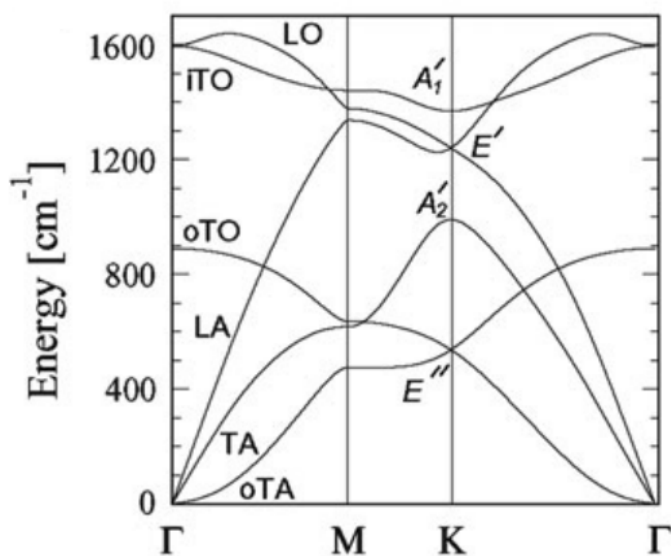
Figure A-3   Phonon dispersion of monolayer graphene [11].

<div align="center">G Band</div>

Single layer graphene satisfies the symmetry operations of D6h point group. The phonons with wavevector q~0 (Γ-point) belongs to E_{2g} and B_{2g} irreducible representation. The E_{2g} is a Raman active mode because the polarization of light can be transformed as Cartesian coordinates [11]. The atomic displacements of E_{2g} at Γ in the single-layer graphene as shown in Figure A-4, are in-plane transverse optical (iTO) and longitudinal optic (LO) phonons [110]. The frequency of these vibrations is ~1580 cm^{-1} and is termed as G band is the Raman spectrum of graphene related systems.

G band is sensitive to the number of graphene layers and its intensity increases in almost linear relation with the number of layers. Intuitively, this can be thought of as more optical phonons are created at Γ-point due increased layers, thus intensifying the peak. Moreover, this band shifts towards the lower energy as the number of layers increase, but it is not an accurate method to characterize graphene layers [111].
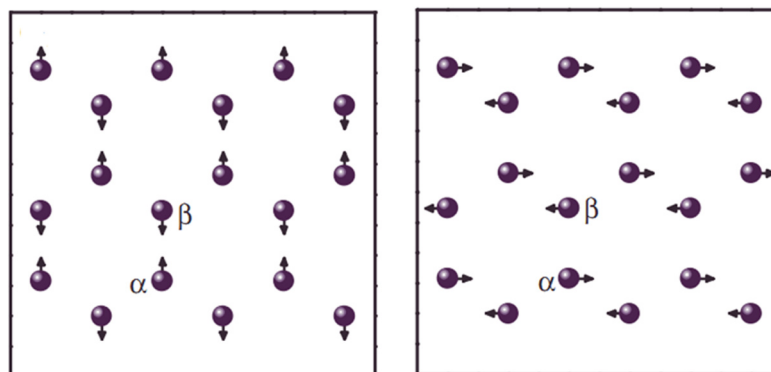
Figure A-4   Schematics of vibrations of iTO and LO modes in the monolayer graphene
at center of brillouin zone, Γ [110].

The peak position and FWHM of G band is also sensitive to doping. Stephene et al. showed the difference in the intensity and FWHM of G band of monolayer graphene suspended and supported on SiO₂. The area map of intensity and FWHM of G peak intensity of supported graphene showed variations, which was attributed to the inhomogeneity due to SiO₂ [112]. On the contrary, the area map of suspended graphene was uniform with the G peak intensity close to the single crystal graphene and the FWHM close to charge neutral graphene. It has also been reported that the doping level can be measured from the frequency shift of the G band, provided density is greater than 6×10^{12} cm⁻² [111].

The frequency of the G band also shifts with the strain, due to the change in the electronic structure. The effect of uniaxial strain was studied by transferring graphene to flexible substrate and the Raman spectrum was taken under various strain conditions. It was observed that redshift in the G band occurs under increased uniaxial strain [111,112].

D Band

The D band is due to disorders in the graphene lattice and is associated with the iTo branch near the K-point [11]. It is due to the single-photon double-resonance inter-valley Raman process, as shown in Figure A-5 (a). The defects can cause elastic scattering of electron which breaks $q \sim 0$ requirement for photons. The second-order process can be explained in four steps: i) The incident photon excites the electron and moves it to a high energy state, ii) the excited electron gets scattered to a state $k - q$ with a phonon emission with wavevector q, iii) if there is a defect in the structure the momentum of electron can be changed back to k, and 4) the electron radiates photon by coming back to its normal state [11]. The atomic vibrations at K due to this mode, having vibrational frequency ~1350 cm^{-1}, is shown in Figure A-5 (b). If the second-order process is intra-valley, the vibration at ~1620 cm-1 occurs and is termed as D′ band, as shown in Figure A-5 (c) [9,11]. The intensity of D′-band is much lesser than D band and is not usually observed in less defective graphene. Therefore, it is not usually considered for characterization.
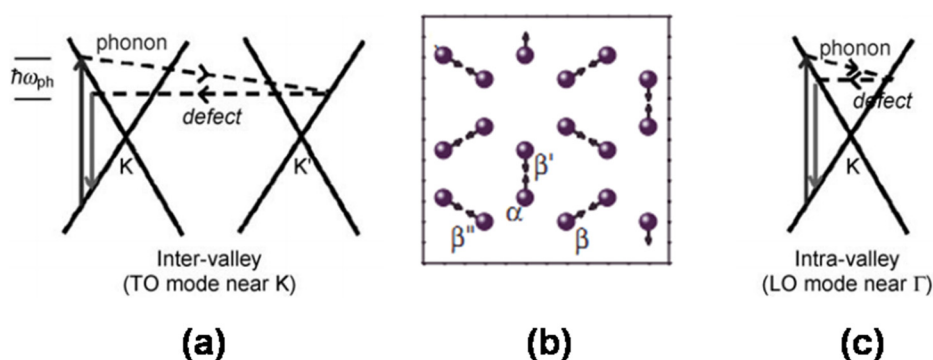
Figure A-5   Origin of D and D′-band in Raman spectrum. (a) One-phone second -order inter-valley process showing the elastic scattering due to defect and thus reason behind D band [11], (b) Motion of atoms at K in the Brillouin zone due to defects [110], (c) One-phone second -order intra-valley process, the origin of D′ band [11].

The D band is dispersive and its peak shifts with the laser energy. A schematics of the basic idea behind the dispersive nature is shown in Figure A-6. With the change of laser energy, the wavevector of the phonon created would change, which results into the peak shift [9,11]. With the increased laser energy a blue shift in the spectrum is observed, as expected.
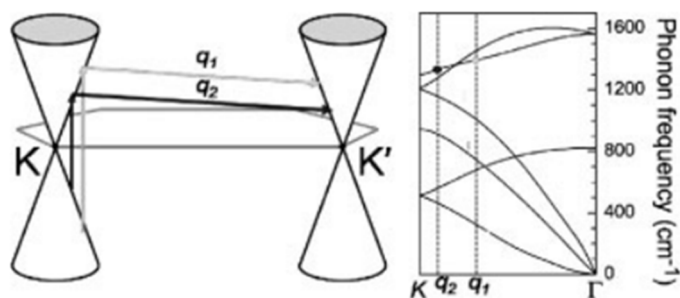
Figure A-6   The origin behind the dispersive nature of second-order Raman processes. the increase in the laser energy ($E_1 > E_2$), the energy of the phonon decreases thus causing a red shift in the Raman spectrum [11].

As graphene is a 2D material, therefore both 0-D and 1-D defects can occur in the lattice structure. 0-D defects are the missing atoms or impurities in the lattice. To study the effect of 0-D defect, Ar^+ ions were bombarded on monolayer graphene, and scanning tunneling microscopy and Raman spectroscopy were correlated. The inter-defect distance L_D was measured from STM and Raman spectroscopy simultaneously. The Raman spectra of monolayer graphene bombarded with Ar^+ ions with different doses are shown in Figure A-7. With 10^3 Ar^+/cm^2, the G peak started to disappear showing the material was losing its signature of graphene. At 10^4 Ar^+/cm^2 the D peak also decreased, predicting the hexagonal structure was not present, which was later confirmed with STM [9,11]. The L_D and I_D/I_G was measure by STM and Raman respectively, and correlated as shown in Figure A-8.
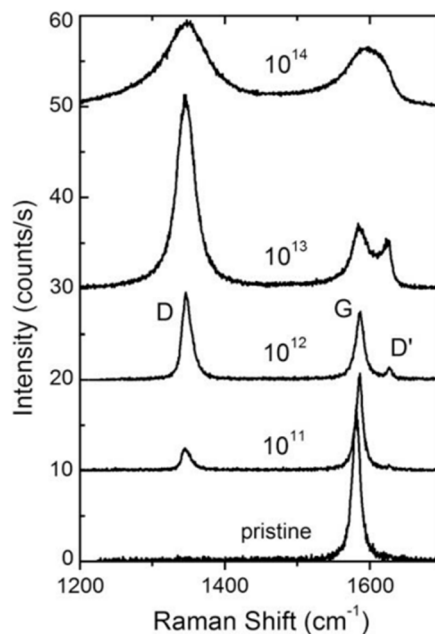
Figure A-7   Evolution of G and D-bands of a monolaye graphene on SiO_2, when subject to Ar^+ ion bombardment. The ion doses are from 10^{11} to 10^{14} Ar^+/cm^2 from bottom to top spectra [11].
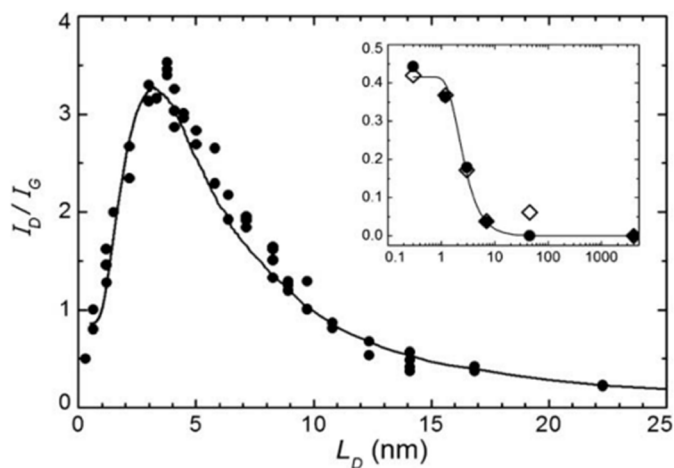
Figure A-8   Correlation between the ratio of peak intensities of D to G band and inter-defect distance calculated from X-Ray diffraction [11].

1-D defects are due to crystalline boundaries and edges in the graphene lattice. Tunistra and Koening measured the in-plane crystal size (L_a) by X-ray diffraction and correlated it to the Raman spectrum. The I_D/I_G ratio was reported to be inversely proportional to L_a. A comprehensive study to develop the relation between I_D/I_G and L_a which was independent of the laser energy was performed by Cancado et al. [80]. The Raman spectra of sample with different L_a, measured from X-ray diffraction peaks, were taken for five different laser energy values, as shown in Figure A-9(a,b). The I_D/I_G was plotted versus $1/L_a$, corresponding to different energies and all the curves collapsed when I_D/I_G axis was scaled by E_{laser}^4, as shown in Figure A-9 (c,d).
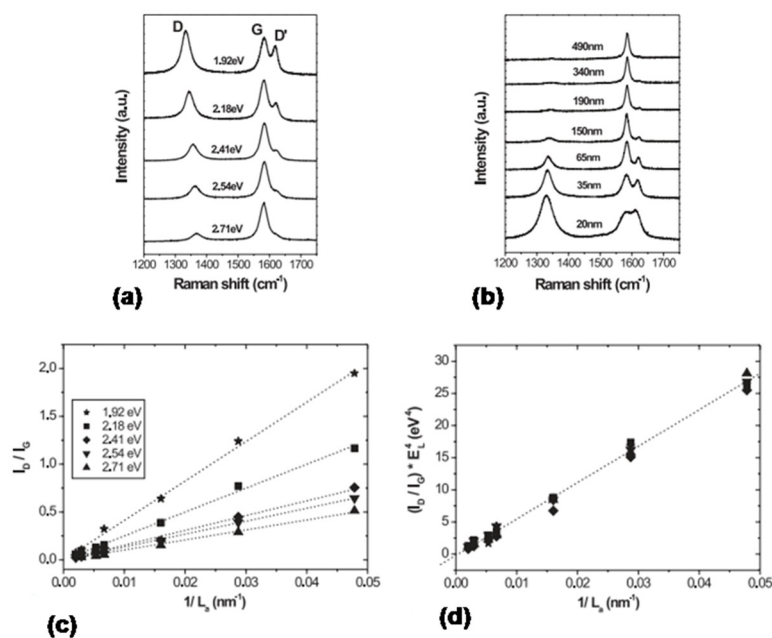
Figure A-9   Effects of first order defects in Raman spectrum of graphene. (a) Raman spectrum of a nanographite heated at 2000 ˚C for five different laser energies, (b) Raman spectrum of nanographite samples with different in-plane crystal sizes taken with 523 nm laser, (c) The ratio of intensities of D to G band is plotted versus $1/L_a$ measure from X-Ray diffraction, (b) All curve in (c) collapsed by scaling axis by Elaser[4] [11].

2D Band

The 2D band is also a second-order band similar to D band, but involves creation of two-phonons with opposite wave vector, to satisfy condition q~0. Therefore it is independent of the defects and occurs at ~2700 cm^{-1}, double the frequency of D band; the reason behind naming it 2D band. The double resonance process for two-phonon Raman scattering is shown in Figure A-10.
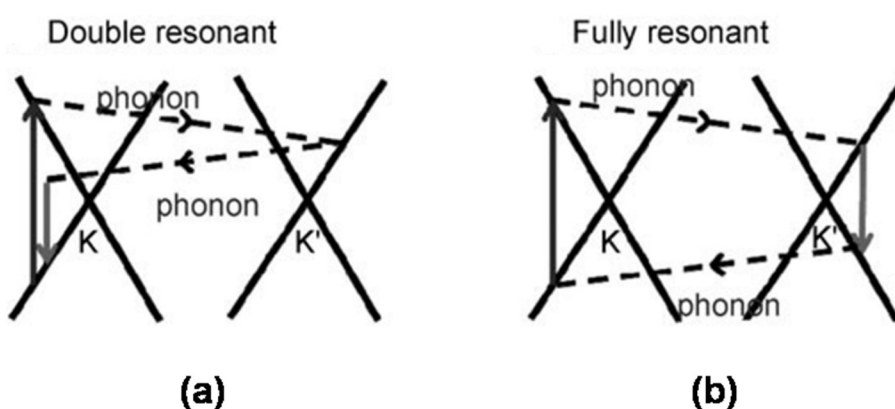
Figure A-10   Second-order two phonon Raman processes, The origin of 2D band. (a) and (b) shows the double resonant and fully resonant processes [11].

The 2D band is also dispersive in nature due to the reasons discussed earlier. The intensity, shape and FWHM of the 2D band are sensitive to the number of layers of graphene [9,11]. The Raman spectra showing the dispersion of 2D band taken under various laser energies is shown in Figure A-11. It has also been reported that the 2D band experiences red (blue) shift with the electron (hole) doping [111]. The FWHM of the 2D band also exhibits broadened FWHM at the doped region. The effect of strain on the 2D band has also been studied. Red shift in the peak of 2D band occurs under strained conditions. As the strain increases, C-C bond elongates which results in weakening the

bond-energy and lowers the vibration frequencies. This results in shifting the peak intensities to lower wavenumber [11,111].
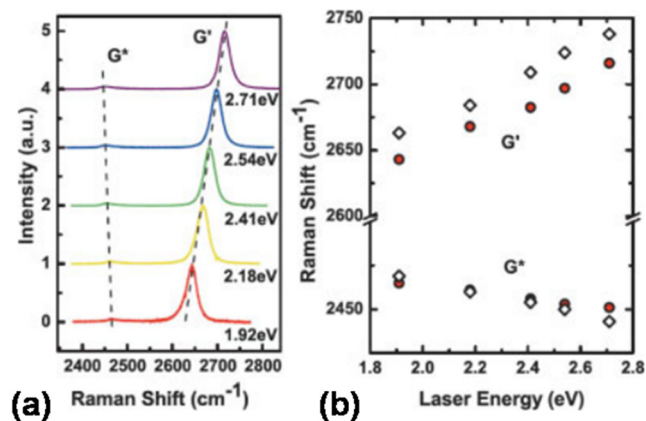
Figure A-11   The evolution of 2D peak with the variation in laser energy. (a) Red shift in the Raman spectrum is observed with the decreases laser energy, (b) Plot of laser energy versus peak-shift taken from part (a) [11].

APPENDIX B

HOME-MADE CHEMICAL VAPOR DEPOSITION

The synthesis carried out in this work was done in a home-made CVD setup. The setup along with the cylinders is shown in Figure B-1. Lindberg/Blue Model Number with 1inch diameter quartz tube is used. In order to ensure purity, all the fittings and the piping in the setup are made of polyvinyl chloride. Moreover, process gasses research grade 5.0 (99.999% purity) were used. The temperature ramp rates from $0 - 700$ ˚C and $700 - 1000$ ˚C were ~50 ˚C/minute and ~25 ˚C, respectively.

Figure B-1   Home-made chemical vapor depostion furnace for the growth of graphene and pyrolytic carbon.

APPENDIX C

SAMPLE PREPARATION FOR CVD

Si wafers (3 inch diameter) with 300 nm thermally grown SiO_2 were used as substrate for Ni films. The wafer was first scribed into strips 0.8 inch wide strips. Before the evaporation of 300 nm Ni, the wafers were cleaned to ensure better adhesion of Ni film and impurity-free synthesis of bilayer graphene and pyrolytic carbon. Following cleaning steps were carried out:

- Acetone dip: 10 minutes

- Methanol dip: 10 minutes

- DI water rinse: 10 minutes

- N_2 dry

- Nanostrip (Commercial Piranha substitute) dip: 20 minutes

- DI Water rinse: 10 minutes

- N_2 dry

To evaporate Ni, Angstrom Engineering electron-beam evaporator was used. The samples were loaded in the chamber and to create ultra-high vacuum (UHV), first rough pump was turned on to create vacuum $\sim 5 \times 10^{-2}$ Torr. Afterwards, cryogenic pump overtook to create UHV. The gasses in the chamber were purged by cryogenic pump cooled with liquid N_2. The evaporation was started after $<1 \times 10^{-7}$ Torr was achieved. Ni pallets in the chamber placed in Alumina crucible (both purchased from International Advanced Materials) were evaporated with the following parameters:

- Electron-beam accelerating voltage: 8.7 kV

- Electron-beam current: 2.07 A

- Power ramp-up rate: 1%/minute

- Evaporation Rate: 0 .1 Å/s

After evaporation was completed, the samples were left in the furnace for at least 30 minutes, before bringing to atmospheric temperature and pressure. Before loading the samples into the CVD furnace, cleaning in ultra-violet ozone (UVO) environment for 2 minutes was done to remove any organic contaminants on the sample during its removal from electron-beam evaporator.

REFERENCES

[1] International Technology Roadmap for Semiconductors. http://www.itrs.net (accessed April 01, 2012)

[2] Geim, A. K.; Novoselov, K. S. The Rise of Graphene. *Nat. Mater.* **2007**, *6*, 183-191.

[3] Novoselov, K. S.; Geim, A. K.; Morozov, S. V.; Jiang, D.; Zhang, Y.; Dubonos, S. V.; Grigorieva, I. V.; Firsov, A. A. Electric Field Effect in Atomically Thin Carbon Films. *Science* **2004**, *306*, 666-669.

[4] Bolotin, K. I.; Sikes, K. J.; Jiang, Z.; Klima, M.; Fudenberg, G.; Hone, J.; Kim, P.; Stormer, H. L. Ultrahigh Electron Mobility in Suspended Graphene. *Solid State Commun.* **2008**, *146*, 351-355.

[5] Moser, J.; Barreiro, A.; Bachtold, A. Current-induced Cleaning of Graphene. *Appl. Phys. Lett.* **2007**, *91*, 163513.

[6] Nair, R. R.; Blake, P.; Grigorenko, A. N.; Novoselov, K. S.; Booth, T. J.; Stauber, T.; Peres, N. M. R.; Geim, A. K. Fine Structure Constant Defines Visual Transparency of Graphene. *Science* **2008**, *320*, 1308.

[7] Lee, C.; Wei, X.; Kysar, J. W.; Hone, J. Measurement of the Elastic Properties and Intrinsic Strength of Monolayer Graphene. *Science* **2008**, *321*, 385-388.

[8] Bunch, J. S.; Verbridge, S. S.; Alden, J. S.; van der Zande, A. M.; Parpia, J. M.; Craighead, H. G.; Mceuen, P. L. Impermeable Atomic Membranes from Graphene Sheets. *Nano Lett.* **2008**, *8*, 2458-2462.

[9] Raza, H., Ed. *Graphene Nanoelectronics: Metrology, Synthesis, Properties and Applications*; Springer: Berlin, 2012.

[10] Raza, H.; Kan, E. C.; Field modulation in bilayer graphene band structure**.** *J Phys Condens Matter* **2009**, *21***,**102202

[11] Jorio, A.; Dresselhaus, M.; Saito, R.; Dresselhaus, G. F. *Raman Spectroscopy in Graphene Related Systems*. Wiley-Vch: New Jersey, 2011.

[12] Ferrari, A. C.; Meyer, J. C.; Scardaci, V.; Casiraghi, C.; Lazzeri, M.; Mauri, F.; Piscanec, S.; Jiang, D.; Novoselov, K. S.; Roth, S. *et al*. Raman Spectrum of Graphene and Graphene Layers. *Phys. Rev. Lett.* **2006**, *97*, 187401.

[13] Ferrari, A. C. Raman Spectroscopy of Graphene and Graphite: Disorder, Electron–Phonon Coupling, Doping and Nonadiabatic Effects. *Solid State Commun.* **2007**, *143*, 47-57.

[14] Dresselhaus, M. S.; Dresselhaus, G.; Saito, R.; Jorio, *A. Phys. Rep.* **2005**, *409*, 47-99.

[15] Poncharal, P.; Ayari, A.; Michel, T.; Sauvajol, J.-L. Raman Spectra of Misoriented Bilayer Graphene. *Phys. Rev. B* **2008**, *78*, 113407.

[16] Das, A.; Chakraborty, B.; Sood, A. K. Raman Spectroscopy of Graphene on Different Substrates and Influence of Defects. *Bull. Mater. Sci.* **2008**, *31*, 579–584.

[17] Blake, P.; Hill, E. W.; Neto, A. H. C.; Novoselov, K. S.; Jiang, D. Making Graphene Visible. *Appl. Phys. Lett.* **2013**, *91*, 063124.

[18] Giannazzo, F.; Sonde, S.; Raineri, V.; Compagnini, G.; Aliotta, F.; Ponterio, R.; Rimini, E. Optical, Morphological and Spectroscopic Characterization of Graphene on SiO2. *Phy. Status Solidi C* **2010**, *7*, 1251-1255.

[19] Chae, S. J.; Gunes, F.; Kim, K. K.; Kim, E. S.; Gang, H. H.; Kim, S. M.; Shin, H-J.; Yoon, S-M.; Choi, J-Y., Park, M. H.; Yang, C. W.; Pribat, D.; Le, Y. H. Synthesis of Large-Area Graphene Layers on Poly-Nickel Substrate by Chemical Vapor Deposition: Wrinkle Formation. *Adv. Mater.* **2009**, *21*, 2328–2333.

[20] Meyer, J. C.; Geim, A. K.; Katsnelson, M. I.; Novoselov, K. S.; Booth, T. J.; Roth, S. The Structure of Suspended Graphene Sheets. *Nature* **2007**, *446*, 60-63.

[21] Rümmeli, M. H.; Rocha, C. G.; Ortmann, F.; Ibrahim, I.; Sevincli, H.; Börrnert, F.; Kunstmann, J.; Bachmatiuk, A.; Pötschke, M.; Shiraishi, M.; Meyyappan, M.; Büchner, V.; Roche, S.; Cuniberti, G. Graphene: Piecing it Together. *Adv. Mater.* **2011**, *23*, 4471-4490.

[22] Li, X.; Cai, W.; Colombo, L.; Ruoff, R. S. Evolution of Graphene Growth on Ni and Cu by Carbon Isotope Labeling**.** *Nano Lett.* **2009**, *9***,** 4268–4272.

[23] Obraztsov, A. N.; Obraztsova, E. A.; Tyurnina, A. V.; Zolotukhin, A. A. Chemical Vapor Deposition of Thin Graphite Films of Nanometer Thickness. *Carbon* **2007**, *45*, 2017-2021.

[24] Yu, Q.; Lian, J.; Siriponglert, S.; Li, H.; Chen, Y. P.; Pei, S-S. Graphene Segregated on Ni Surfaces and Transferred to Insulators. *Appl. Phys. Lett.* **2008**, *93***,** 113103.

[25] Kim, K. S.; Zhao, Y.; Jang, H.; Lee, S. Y.; Kim, J. M.; Kim, K. S.; Ahn, J-H.; Kim, P.; Choi, J-Y.; Hong, B. H. Large-Scale Pattern Growth of Graphene Films for Stretchable Transparent Electrodes. *Nature* **2009**, *457***,** 706–710.

[26] Reina, A.; Jia, X.; Ho, J.; Nezich, D.; Son, H.; Bulovic, V.; Dresselhaus, M. S.; Kong, J. Large Area, Few-Layer Graphene Films on Arbitrary Substrates by Chemical Vapor Deposition. *Nano Lett.* **2009**, *9*, 30-35.

[27] Lee, Y;, Bae S., Jang, H.; Jang, S.; Zhu, S-E.; Sim, S.H.; Song, Y.I.; Hong, B. H.; Ahn, J-H. Wafer-Scale Synthesis and Transfer of Graphene Films. *Nano Lett.* **2010**, *10***, 490-493.

[28] Zhang, Y.; Gomez, L.; Ishikawa, F. N.; Madaria, A.; Ryu, K; Wang; Badmaev,; Zhou, C. W. Comparison of Graphene Growth on Single-Crystalline and Polycrystalline Ni by Chemical Vapor Deposition. *J. Phys. Chem. Lett.* **2010**, *1*, 3101-3107.

[29] Li, X.; Zhu, Y.; Cai, W.; Borysiak, M.; Han, B.; Chen, D.; Piner, R. D.; Colombo, L.; Ruoff, R. S. Transfer of Large-Area Graphene Films for High-Performance Transparent Conductive Electrodes. *Nano Lett.* **2009**, *9*, 4359-63.

[30] Bae, S.; Kim, H.; Lee, Y.; Xu, X.; Park, J.-S.; Zheng, Y.; Balakrishnan, J.; Lei, T.; Kim, H. R.; Song, Y. I. *et al.* Roll-to-Roll Production of 30-inch Graphene Films for Transparent Electrodes. *Nat.Nanotechnol.* **2010**, *5*, 574-8.

[31] Schwierz, F. Graphene Transistors. *Nat. Nanotechnol.* **2010**, *5*, 487-496.

[32] Reddy, D.; Register, L. F.; Carpentyer,G , D.;Banerjee, S. K. Graphene Field-effect Transistors. *J. Phys. D: Appl. Phys.* **2011**, *44*, *313001*.

[33] Raza, H. Electronic Structure Modulation for Low-Power Switching. *Nanoscale Res. Lett.* **2012**, *8*, 74.

[34] Chen, Y.; Zhang, B.; Liu, G.; Zhuang, X.; Kang, E.; Graphene and its Derivatives: Switching ON and OFF. *Chem. Soc. Rev.* **2011**, *41*, 4688-4707 and references there-in.

[35] Mojarabian, F. M.; Rashedi, G. GMR Effects in Graphene-Based Ferromagnetic/Normal/Ferromagnetic Junctions. *Physica E* **2011**, *44*, 647-653.

[36] Di, C. A.; Wei, D. C.; Yu, G.; Liu, Y.Q .; Guo, Y.L. ; Zhu, D. B. Patterned Graphene as Source/Drain Electrodes for Bottom-Contact Organic Field-Effect Transistors. *Adv. Mater.* **2008**, *20*, 3289-3294.

[37] Pang, S.; Tsao, H. N.; Feng, X.; Müllen, K. Patterned Graphene Electrodes from Solution-Processed Graphite Oxide Films for Organic Field-Effect Transistors. *Adv. Mater.* **2009**, *21*, 3488-3491.

[38] Lee, W. H.; Park, J.; Sim, S. H.; Jo, S. B.; Kim, K. S.; Hong, B. H.; Cho, K. Transparent Flexible Organic Transistors Based on Monolayer Graphene Electrodes on Plastic. *Adv. Mater.* **2011**, *23*, 1752-1756.

[39] Lee, S.; Jo, G.; Kang, S.-ju; Wang, G.; Choe, M.; Park, W.; Kim, D.-yu; Kahng, Y. H.; Lee, T. Enhanced Charge Injection in Pentacene Field-Effect Transistors with Graphene Electrodes. *Adv. Mater.* **2011**, *23*, 100-105.

[40] Lee, W.; Jo, G.; Lee, S.; Park, J.; Jo, M.; Lee, J.; Jung, S.; Kim, S.; Shin, J.; Park, S. *et al.* Nonvolatile Resistive Switching in $Pr_{0.7}Ca_{0.3}MnO_3$ Devices Using Multilayer Graphene Electrodes. *Appl. Phys. Lett.* **2011**, *98*, 032105.

[41] Yu, W. J.; Chae, S. H.; Lee, S. Y.; Duong, D. L.; Lee, Y. H. Ultra-Transparent , Flexible Single-walled Carbon Nanotube Non-volatile Memory Device with an Oxygen-decorated Graphene Electrode. *Adv. Mater.* **2011**, *23*, 1889-1893.

[42] Ji, Y.; Lee, S.; Cho, B.; Song, S.; Lee, T. Flexible Organic Memory Devices with Multilayer Graphene Electrodes. *ACS Nano* **2011**, *5*, 5995-6000.

[43] Jo, G.; Choe, M.; Lee, S.; Park, W.; Kahng, Y. H.; Lee, T. The Application of Graphene as Electrodes in Electrical and Optical Devices. *Nanotechnol.* **2012**, *23*, 112001.

[44] Fujita, M.; Wakabayashi, K.; Nakada, K.; Kusakabe, K. Localized States at Zig-zag Edges. *J. Phys. Soc. Jpn.* **1996**, *65***,** 1920-1923.

[45] Nakada, K.; Fujita M.; Dresselhaus, G.; Dresselhaus, M. S. Edge State in Graphene Ribbons: Nanometer Size Effect and Edge Shape Dependence. *Phys. Rev. B.* **1996**, *54***,** 17954-17961.

[46] Wakabayashi, K.; Fujita, M.; Ajiki, H.; Sigrist, M. Electronic and Magnetic Properties of Nanographite Ribbons. *Phys. Rev. B* **1999**, *59***,** 8271-8282.

[47] Raza, H.; Kan, E. C. Armchair Graphene Nanoribbons: Electronic Structure and Electric-Field Modulation. *Phys. Rev. B* **2008**, *77***,** 245434.

[48] Raza, H. Zigzag Graphene Nanoribbons: Bandgap and Midgap State Modulation. *J. Phys. Condens. Matter* **2011**, *23***,** 382203.

[49] Raza, H. Edge and Passivation Effects in Armchair Graphene Nanoribbons. *Phys. Rev. B* **2011**, *84***,** 165425.

[50] McCann, E.; Abergel, D. S. L.; Fal'ko, V. I. Electrons in Bilayer Graphene**.** *Solid State Commun.* **2007**, *143,* 110-115.

[51] Castro, E.; Novoselov, K.; Morozov, S.; Peres, N.; Dos Santos, J.; Nilsson, J.; Guinea, F.; Geim, A.; Neto, A. Biased Bilayer Graphene: Semiconductor with a Gap Tunable by the Electric Field Effect. *Phys. Rev. Lett.* **2007**, *99***,** 216802.

[52] Castro Neto, A. H.; Peres, N. M. R.; Novoselov, K. S.; Geim, A. K. The Electronic Properties of Graphene. *Rev. Mod. Phys.* **2009**, *81***,** 109-162.

[53] Ohta, T.; Bostwick, A.; Seyller, T.; Horn, K.; Rotenberg, E. Controlling the Electronic Structure of Bilayer Graphene. *Science* **2006**, *313*, 951-954.

[54] Oostinga, J. B.; Heersche, H. B.; LiuX.; Morpurgo, A. F.; Vandersypen, L. M. K. Gate-Induced Insulating State in Bilayer Graphene Device. *Nat. Mater.* **2008**, *7*, 151-157.

[55] Li, X.; Cai, W.; An, J.; Kim, S.; Nah, J.; Yang, D.; Piner, R.; Velamakanni, A.; Jung, I.; Tutuc, E.; Banerjee, S. K.; Colombo, L.; Ruoff, R. S. Large-Area Synthesis of High-Quality And Uniform Graphene Films on Copper Foils. *Science* **2009**, *324*, 1312-1314.

[56] Wan, D.; Lin, T.; Bi, H.; Huang, F.; Xie, X.; Chen, I-W.; Jiang, M. Autonomously Controlled Homogenous Growth of Wafer-Sized High-Quality Graphene via a Smart Janus Substrate. *Adv. Funct. Mater.* **2012**, *22***,** 1033-1039.

[57] Sun, Z.; Yan, Z.; Yao, J.; Beitler, E.; Zhu, Y.; Tour, J. M. Growth of Graphene from Solid Carbon Sources. *Nature* **2010**, *468***,** 549-552.

[58] Shin, H-J.; Choi, WM.; Yoon, S-M.; Han, G. H.; Woo, Y. S.; Kim, E. S.; Chae, S. J.; Li, X-S.; Benayad, A.; Loc, D. D.; Gunes, F.; Lee, Y. H.; Choi, J-Y. Transfer-Free Growth of Few-Layer Graphene by Self-Assembled Monolayers. *Adv. Mater.* **2011**, *23***,** 4392-4397.

[59] Sabki, S.N.; Garfitt, J.M.; Capiod, P.; Beton, P. H. Graphene Formation by Decomposition of C_{60}. *J. Phys. Chem.* **2011**, *115***,** 7472-7476.

[60] Miyata, Y.; Kamon, K.; Ohashi, K.; Kitaura, R.; Yoshimura, M.; Shinohara, H. A Simple Alcohol-Chemical Vapor Deposition Synthesis of Single-Layer Graphenes Using Flash Cooling. *Appl. Phys. Lett.* **2010**, *96***,** 263105.

[61] Liu, W.; Chung, C-H.; Miao, C-Q.; Wang, Y-J.; Li, B-Y.; Ruan, L-Y.; Patel, K.; Park, Y-J.; Woo, J.; Xie, Y-H. Chemical Vapor Deposition of Large Area Few Layer Graphene on Si Catalyzed with Nickel Films. *Thin Solid Films* **2010**, *518***,** S128-S132.

[62] Zhou, Q.; Lin, L.; Synthesis of Graphene Using Micro Chemical Vapor Deposition. In *IEEE 23rd International Conference on Micro Electro Mechanical Systems: January 24-28, 2010; Wanchai*. New York: IEEE; 2010:43–46.

[63] Shelton, J. C.; Patil, H. R.; Blakely, J. M.; Equilibrium Segregation of Carbon to a Nickel (111) Surface: A Surface Phase Transition. *Surf. Sci.* **1974**, *43***,** 493-520.

[64] Peng, Z.; Yan, Z.; Sun, Z.; Tour, J. M. Direct Growth of Bilayer Graphene on SiO_2 Substrates by Carbon Diffusion through Nickel. *ACS Nano* **2011**, *5***,** 8241-8247.

[65] Malard, L. M.; Pimenta, M. A.; Dresselhaus, G.; Dresselhaus, M. S. Raman Spectroscopy in Graphene. *Phys. Rep.* **2009**, *473***,** 51-87.

[66] McEvoy, N.; Peltekis, N.; Kumar, S.; Rezvani, E.; Nolan, H.; Keele, G. P.; Blau, W. J.; Duesberg, G. S. Synthesis and Analysis of Thin Conducting Pyrolytic Carbon Films. *Carbon* **2012**, *50*, 1216-1226.

[67] Keeley, G. P.; McEvoy, N.; Kumar, S.; Peltekis, N.; Mausser, M.; Duesberg, G. S. Thin Film Pyrolytic Carbon Electrodes: A New Class of Carbon Electrode for Electroanalytical Sensing Applications. *Electrochem. Commun.* **2010**, *12*, 1034-1036.

[68] Aichmayr, G.; Avellan, A.; Duesberg, G. S.; Kreupl, F.; Kudelka, S.; Liebau, M. Carbon/high-k Trench Capacitor for the 40 nm DRAM Generation. In: IEEE Symposium on VLSI Technology; 2007; p. 186-7.

[69] Graham, A. P.; Richter, K.; Jay, T.; Weber, W.; Knebel, S.; Schroder, U. et al. An Investigation of the Electrical Properties of Metal- Insulator-Silicon Capacitors with Pyrolytic Carbon Electrodes. *J. Appl. Phys.* **2010**, *108*, 104508.

[70] Basu, R. N.; Altin, O.; Mayo, M. J.; Randall, C. A.; Eser, S. Pyrolytic Carbon Deposition on Porous Cathode Tubes and Its Use as an Interlayer for Solid Oxide Fuel Cell Zirconia Electrolyte Fabrication. *J. Electrochem. Soc.* **2001**, *148*, A506-A512.

[71] Behzadi, S.; Imani, M.; Yousefi, M.; Galinetto P.; Simchi, A.; Amiri, H.; Stroeve, P.; Mahmoudi, M. Pyrolytic Carbon Coating For Cytocompatibility of Titanium Oxide Nanoparticles: A Promising Candidate for Medical Applications. *Nanotechnology* **2012**, *23*, 045102.

[72] Lucas., P; Marchand, A. Pyrolytic Carbon Deposition from Methane - An Analytical Approach to the Chemical Process. *Carbon* **1990**, *28*, 207-219.

[73] Hu, Z.J.; Zhang, W.G.; Huttinger, K.J.; et al. Influence of Pressure, Temperature and Surface Area/Volume Ratio on the Texture of Pyrolytic Carbon Deposited From Methane. *Carbon* **2003**, *41*, 749-758.

[74] Knight, D. S.; White, W. B. Characterization of Diamond Films by Raman Spectroscopy. *J. Mater. Res.* **1989**, 4, 385-389.

[75] Cancado, L. G.; Takai, K.; Enkoi, T.; Endo, M.; Kim, Y. A.; Mizusaki, H.; Jorio, A. et al. General Equation for the Determination of the Crystallite Size L_a of Nanographite by Raman Spectroscopy. *Appl. Phys. Lett.* **2006**, *88*, 163106.

[76] Umair, A.; Raza, H. Controlled Synthesis of Bilayer Graphene on Nickel. *Nanscale. Res. Lett.* **2012**, *7*, 437.

[77] López-Honorato, E.; Meadows, P. J.; Shatwell, R. A.; Xiao, P. Characterization of the Anisotropy of Pyrolytic Carbon by Raman spectroscopy. *Carbon* **2010**; *48*, 881-90.

[78] Vallerot, J. M.; Bourrat, X.; Mouchon, A.; Chollon, G. Quantitative Structural and Textural Assessment of Laminar Pyrocarbons through Raman Spectroscopy, Electron Diffraction and Few Other Techniques. *Carbon* **2006**; *44*, 1833–1844.

[79] Jawhari, T.; Roid, A.; Casado, J. Raman-Spectroscopic Characterization of Some Commercially Available Carbon-Black Materials. *Carbon* **1995**, *33*, 1561-1565

[80] Bacsa, W.S.; Lannin, J. S.; Pappas, D. L.; Cuomo, J. J. Raman Scattering of Laser-Deposited Amorphous Carbon. *Phys. Rev. B.* **1993,** *47*, 10931-10934.

[81] Möller, S.; Perlov, C.; Jackson, W.; Taussig, C.; Forrest, S. R. A Polymer/semiconductor Write-once Read-many-times Memory. *Nature* **2003**, *426*, 166-169.

[92] Majumdar, H. S.; Baral, J. K.; Österbacka, R.; Ikkala, O.; Stubb, H. Fullerene-based Bistable Devices and Associated Negative Differential Resistance Effect. *Org. Electro.* **2005**, *6*, 188-192.

[83] Scott, J. C.; Bozano, L. D. Nonvolatile Memory Elements Based on Organic Materials. *Adv. Mater.* **2007**, *19*, 1452-1463.

[84] Luo, Y.; Collier, P. C.; Jeppesen, J. O.; Nielsen, K. A.; Delonno, E.; Ho, G.; Perkins, J.; Tseng, H.-R.; Yamamoto, T.; Stoddart, J. F.; Heath, J. R. Two-dimensional Molecular Electronics Circuits. *ChemPhysChem.* **2002**, *3*, 519-525.

[85] Kügeler, C.; Meier, M.; Rosezin, R.; Gilles, S.; Waser, R. High Density 3D Memory Architecture Based on the Resistive Switching Effect. *Solid-State Electronics* **2009**, *53*, 1287-1292.

[86] Dietrich, S.; Angerbauer, M.; Ivanov, M.; Gogl, D.; Hoenigschmid, H.; Kund, M.; Liaw, C.; Markert, M.; Symanczyk, R.; Altimime, L. *et al.* A Nonvolatile 2-Mbit CBRAM Memory Core Featuring Advanced Read and Program Control. *IEEE J. Solid-State Circuits* **2007**, *42*, 839-845.

[87] Prime, D.; Paul, S. Overview of Organic Memories. *Philos. Trans. R. Soc. London, Ser A* **2009,** *367*, 4141-4157.

[88] Brito, B. C. de; Smits, E. C. P.; Hal, P. a. van; Geuns, T. C. T.; Boer, B. de; Lasance, C. J. M.; Gomes, H. L.; Leeuw, D. M. de Ultralow Power Microfuses for Write-Once Read-Many Organic Memory Elements. *Adv. Mater.* **2008**, *20*, 3750-3753.

[89] Zhuang, X.-D.; Chen, Y.; Li, B.-X.; Ma, D.-G.; Zhang, B.; Li, Y. Polyfluorene-Based Push−Pull Type Functional Materials for Write-Once-Read-Many-Times Memory Devices. *Chem. Mater.* **2010**, *22*, 4455-4461.

[90] Ohira, a.; Okoshi, K.; Fujiki, M.; Kunitake, M.; Naito, M.; Hagihara, T. Versatile Helical Polymer Films: Chiroptical Inversion Switching and Memory with Re-Writable (RW) and Write-Once Read-Many (WORM) Modes. *Adv. Mater.* **2004**, *16*, 1645-1650.

[91] Ouyang, J.; Chu. C-W.; Sieves, D.; Yang, Y. Electric-Field-Induced Charge Transfer between Gold Nanoparticle and Capping 2-Naphthalenethiol and Organic Memory Cells. *Appl. Phys. Lett.* 2005, **86**, *123507*.

[92] Schottky, W. Discrepencies in Ohm's Laws in Semiconductors. *Phys. Z.* **1940**, *41*, 570-573.

[93] Bardeen, J. Surface States and Rectification of Metal Semi-Conductor Contact. *Phys. Rev.* **1947**, *71*, 717-727.

[94] Heine, V. Theory of Surface States. *Phys. Rev.* **1956**, *138*, A1689-A1696.

[95] Datta, S. Quantum Transport: Atom to Transistor. Cambridge: *Cambridge University Press*; **2005**.

[96] Meir, Y.; Wingreen, N. S. Landauer Formula for the Current through an Interacting Electron Region. *Phys. Rev. Lett.* **1992**, *68*, 2512-2515.

[97] Chen, Z.; Appenzeller, J.; Knoch, J.; Lin Y-M.; Avouris, P. The Role of Metal−Nanotube Contact in the Performance of Carbon Nanotube Field-Effect Transistors. *Nano Lett.* **2005**, *5*, 1497-1502.

[98] Raza, H.; Kan, E. C. An Atomistic Quantum Transport Solver with Dephasing for Field-Effect Transistors. *J. Comp. Elec.* **2008**, *7*, 423-426.

[99] Ohring, M. Reliability and Failure of Electronic Material and Devices. Waltham: A*cademic Press*, **1998**.

[100] Neto, C.; A. H.; Peres, N. M. R.; Novoselov, K. S.; Geim A. K. The Electronic Properties of Graphene. *Rev. Mod. Phys.* **2009**, *81*, 109-162.

[101] MaLevendorf, M, P.; Kim, C-J.;Brown, L.; Huang, P. Y.;Havener, R. W.; Muller, D, A.; Park, J. Graphene and Boron Nitride Lateral Heterostructures for Atomically Thin Circuitry. *Nature* **2012,** *488*, 627–632.

[102] Schettino, V.; Pagliai, M.; Ciabini, L.; Cardini, G. The Vibrational Spectrum of Fullerene C_{60}. *J. Phys. Chem. A.* **2001**, *105*, 11192-11196.

[103] Kuzmany, H.; Pfeiffer, R.; Hulman, M.; Kramberger, C. Raman Spectroscopy of Fullerenes and Fullerene–Nanotube Composites. *Philos. Trans. R. Soc. London Ser. A* **2004**, *362*, 2375–2406.

[104] Sun, Y.N.; Feldman, A.; Farabaugh, E. N. X-ray Photoelectron Spectroscopy of O 1s and Si 2p Lines in Films of SiO_x Formed by Electron Beam Evaporation. *Thin Solid Films* **1988** *157*, 351-360.

[105] Siebeneicher, P.; Kleemann, H.; Leo, K.; Lüssem, B. Non-volatile Organic Memory Devices Comprising SiO_2 and C_{60} Showing 10^4 Switching Cycles. *Appl. Phys. Lett.* **2012**, *100*, 193301.

[106] He, J.; Chen, B. O.; Flatt, A. K.; Stephenson, J. J.; Doyle, C. D.; Tour, J. M. Metal-Free Silicon–Molecule–Nanotube Testbed and Memory Device. *Nat. Mater.* **2006**, *5*, 63-68.

[107] Umair, A.; Raza, T. Z.; Raza, H. On the Crystal Size Studies of Pyrolytic Carbon by Raman Spectroscopy. http://arxiv.org/abs/1303.6364.

[108] Umair, A.; Raza, T. Z.; Raza, H. Molecular Memory with Atomically-Smooth Graphene Contacts. http://arxiv.org/abs/1303.6603.

[109] Hou, T-H.; Raza, H.; Afshari, K.; Ruebusch, D. J.; Kan, E. C. Nonvolatile Memory With Molecule-Engineered Tunneling Barriers. *Appl. Phys. Lett.* **92**, 153109.

[110] Yan, J., Zhang, Y., Kim, P., and Pinczuk, A. Electric Feld Effect Tuning of Electron-Phonon Coupling in Graphene. *Phys. Rev. Lett.* **2007**, *98*, 166802-166805.

[111] Tang, B.; Guoxin, H.; Gao, Hanyang. Raman Spectroscopic Characterization of Graphene. *Appl. Spectro. Rev.* **2010**, *45,* 369-407.

[112] Stephane, B.; Sunmin, R.; and Louis, E. Probing the intrinsic properties of exfoliated graphene: Raman spectroscopy of free-standing monolayers. *Nano Lett.* **2009**, *9*, 346-352.